Los Alamos NATIONAL LABORATORY EST.1943

LA-UR-19-27741 (Accepted Manuscript)

MPRAD: A Monte Carlo and ray-tracing code for the proton radiography in high-energy-density plasma experiments

Lu, Yingchao
Li, Hui
Flippo, Kirk Adler
Kelso, Kwyntero Van
Liao, Andy Sha
Li, Shengtai
Liang, Edison P.

Provided by the author(s) and the Los Alamos National Laboratory (2020-03-03).

To be published in: Review of Scientific Instruments

DOI to publisher's version: 10.1063/1.5123392

Permalink to record: http://permalink.lanl.gov/object/view?what=info:lanl-repo/lareport/LA-UR-19-27741

Disclaimer:
Los Alamos National Laboratory, an affirmative action/equal opportunity employer, is operated by Triad National Security, LLC for the National Nuclear Security Administration of U.S. Department of Energy under contract 89233218CNA000001. By approving this article, the publisher recognizes that the U.S. Government retains nonexclusive, royalty-free license to publish or reproduce the published form of this contribution, or to allow others to do so, for U.S. Government purposes. Los Alamos National Laboratory requests that the publisher identify this article as work performed under the auspices of the U.S. Department of Energy. Los Alamos National Laboratory strongly supports academic freedom and a researcher's right to publish; as an institution, however, the Laboratory does not endorse the viewpoint of a publication or guarantee its technical correctness.

RESEARCH LIBRARY

ACCEPTED MANUSCRIPT
Review of Scientific Instruments
This is the author's peer reviewed, accepted manuscript. However, the online version of record will be different from this version once it has been copyedited and typeset.
PLEASE CITE THIS ARTICLE AS DOI:10.1063/1.5123392
AIP Publishing

MPRAD: A Monte Carlo and ray-tracing code for the proton radiography in high-energy-density plasma experiments

Yingchao Lu,[1,2,*] Hui Li,[1] Kirk A. Flippo,[1] Kwyntero Kelso,[1] Andy Liao,[1] Shengtai Li,[1] and Edison Liang[2]

[1] *Los Alamos National Laboratory, Los Alamos, New Mexico, 87545, USA*
[2] *Department of Physics and Astronomy, Rice University, Houston, Texas 77005, USA*

(Dated: November 20, 2019)

Proton radiography is used in various high-energy-density (HED) plasma experiments. In this paper, we describe a Monte Carlo and ray-tracing simulation tool called MPRAD that can be used for modeling the deflection of proton beams in arbitrary three dimensional electromagnetic fields, as well as the diffusion of the proton beams by Coulomb scattering and stopping power. The Coulomb scattering and stopping power models in cold matter and fully ionized plasma are combined using interpolation. We discuss the application of MPRAD in a few setups relevant to HED plasma experiments where the plasma density can play a role in diffusing the proton beams and affecting the prediction and interpretation of the proton images. It is shown how the diffusion due to plasma density can affect the resolution and dynamical range of the proton radiography.

Keywords: Monte Carlo, ray-tracing, proton radiography

I. INTRODUCTION

Proton radiography[1, 2] is a diagnostic tool for time-resolved and spatial-resolved studies of the electromagnetic field structures in inertial confinement fusion (ICF) and high energy density (HED) plasmas. The information about the morphology and strengths of electric and magnetic field is coded in the deflection angle of the proton beams and alters the proton flux after interaction with electromagnetic field. The proton flux is then recorded on a detector. This kind of imaging technique has been used to characterize the electromagnetic fields and carry out measurements in a variety of experiments, including ICF implosion capsules[3–12], magnetic reconnection[13–18], self-generated magnetic fields through Biermann battery term[19–25] and plasma instabilities[26–33], non-ideal MHD effects[34–36], and laboratory dynamo experiments[37, 38].

In ICF and HED experiments, two distinct types of proton sources have been developed for high performance diagnostics. First, in a capsule implosion, DD(3MeV) and D^3He(14.7MeV) protons from fusion reaction driven by multiple laser beams. The protons leave tracks in CR-39[1, 39] which is etched and scanned to get the absolute location and track characteristics of each proton [39]; Second, broadband proton beams[2, 40] up to 60MeV are driven by ultra-intense ($> 10^{18}$W/cm^2) short pulse laser beam through Target Normal Sheath Acceleration (TNSA) mechanism, and the proton flux is recorded on the radiochromic film pack with a sequence of proton energies. In general, the TNSA proton backlighter offers better spatial and temporal resolution, while the D^3He fusion-based techniques offers better spatial uniformity and energy resolution.

The understanding of field structure from proton images is limited by the fact that the images are a two dimensional mapping of the three dimensional field distribution. The general mapping can be nonlinear, degenerate and diffusive. Direct interpretation of the proton images is achievable only under the assumptions of simple field geometries. Some inverse-problem type of general techniques[41–43] have been developed to infer the integral quantities over the line of sight, e.g., magnetic field perpendicular to line of sight ($\int d\boldsymbol{z} \times \boldsymbol{B}$) or MHD current along the line of sight ($\int d\boldsymbol{z} \cdot \nabla \times \boldsymbol{B}$). The comprehensive description of the inverse-problem type of techniques for proton images of stochastic magnetic fields has been developed[42]. However, the caustic and diffusive regimes are still challenging for inferring the fields. The primary focus of this paper to develop a tool to understand the proton image in the diffusive regime, where a ballistically propagating beam from the source is diffused by Coulomb scattering and stopping power.

There are some general-purpose Monte Carlo toolkits, e.g. MCNP[44] and GEANT4[45], and tools specifically for HED applications[46, 47], for forward modeling of proton radiography. MCNP and GEANT4 have the features to model the energy lost and collisional scattering of protons in cold matter, but corrections are needed for calculations of plasma stopping power and scattering angle[48]. In this paper, we take those corrections related to plasma into account and develop a more accurate Monte Carlo and ray-tracing tool called MPRAD(multi-MeV proton radiography) for forward modeling of proton radiography. We make some approximations in the models for Coulomb scattering and stopping power used in the code. Those are good approximations under the condition that proton energy $E_p > 1$MeV, electron temperature $\frac{kT_e}{545\text{eV}} < E_p$[MeV], density $\rho/A \ll 10^4$g/cc (A is the mass number of the matter), and the transition layer between cold matter and fully ionized plasma is thin compared to the rest of the system. This condition covers the conditions of a range of ICF and HED experiments. MPRAD is written in Python with MPI+OpenMPI parallelization among particles or rays, using Cython and

* yclu@lanl.gov

ACCEPTED MANUSCRIPT
Review of Scientific Instruments
This is the author's peer reviewed, accepted manuscript. However, the online version of record will be different from this version once it has been copyedited and typeset.
PLEASE CITE THIS ARTICLE AS DOI:10.1063/1.5123392
AIP Publishing

MPI4py package. Cython compilation for the core part of the code is used to improve the performance. The output data from plasma-dynamical modeling such as radiation-magnetohydrodynamics or particle-in-cell(PIC) simulations can be imported into MPRAD. The Python package from Yt-project[49] is used to read the data from FLASH[50] simulations. Each MPI process gets the whole data set of pre-calculated quantities. Each thread solves the Monte Carlo transport for each particle (or ray transport for each ray) independently. And the binned data (or final quantities for the rays) is collected after each process and thread completes the calculation for the targeted number of particles(or rays). The process for making MPRAD an open source code is ongoing. Our tool will be used for designing and analyzing the data for the recent OMEGA experiments of magnetic field generation in shock-shear type of targets[51].

This paper is organized as follows. Sec II describes the features of the MPRAD code, including the model for Coulomb scattering and stopping power. In Sec III we perform benchmark simulations for cold matter with MPRAD and compare the results with MCNP simulations. Some applications and examples for the effect of diffusion process on the proton radiography are discussed in Sec IV. The summary is given in Sec V.

II. FEATURES OF THE CODE

In MPRAD, we solve the relativistic equation of proton motion, i.e. the evolution of position and velocity of the protons in the beam, in electromagnetic field, similar to the features in the existing tools[41, 44, 45, 47]. In addition we implement the stopping power and Coulomb Scattering, both in cold matter approximation and weakly interacting plasmas. Pre-calculated quantities are used to speed up the large scale simulations.

A. Stopping power

In MPRAD code, we use the models for stopping power and energy-loss straggling in the literatures[52–56]. The relativistic effects of protons are taken into account to accurately calculate the motion of non-relativistic to highly relativistic protons with $\beta = v/c$, where v is the velocity of the proton, and c is the speed of light. The velocity for the proton beam is assumed to be much higher than the electron thermal speed $v_p > v_{e,th}$, which implies $\frac{E_p/m_p}{kT_e/m_e} > 1$, i.e.

$$\frac{kT_e}{545\text{eV}} < \frac{E_p}{1\text{MeV}} \tag{1}$$

Under the $v_p > v_{e,th}$ assumption, we further assume that the beam–plasma coupling strength[55] γ_c is small, i.e.

$$\gamma_c = 6.8\times10^{-3}\frac{(\frac{\rho}{1\text{g/cc}})^{1/2}}{(\frac{E_p}{1\text{MeV}})^{3/2}A^{1/2}} \ll 1 \tag{2}$$

where A is the mass number of the matter. For $E_p >$ 1MeV and $\rho/A \ll 10^4$g/cc, γ_c is always much less than unity, so that the beam–plasma coupling effect can be neglected[55].

For room temperature, we use the stopping power for cold matter. For proton energy $E_p > 1$MeV, the stopping power in cold matter can be written as[52]

$$\begin{aligned}\frac{d\langle E_p\rangle}{dx} &= -\frac{4\pi e^4 n_e}{\beta^2 m_e c^2}\Big[f(\beta)+a\Big] \\ &= -\frac{0.31\text{MeV/cm}\times Z\frac{\rho}{1\text{g/cc}}}{A\beta^2}\Big[f(\beta)+a\Big]\end{aligned} \tag{3}$$

where m_e is the mass of electron, n_e is the total electron number density(including both free electrons and bound electrons), ρ is the density of the matter, A is the mass number of the matter, and Z is the charge number of the matter. The bracket $\langle E_p\rangle$ represents the average energy lost, and x is the path length of the proton. Due to the fact that the collision between the protons and the particles in the matter is random, the energy lost follows a distribution deviating from the average energy lost, which is described as the straggling function as given in Eq(13). The quantity a is related to the material property and can be found in stopping power database such as PSTAR [57] and SRIM[58]. The function $f(\beta)$ is

$$f(\beta) = \ln[\beta^2/(1-\beta^2)] \tag{4}$$

For mixture, compound or isotopes, i.e. different A's and Z's, the stopping power is

$$\frac{d\langle E_p\rangle}{dx} = -\frac{0.31\text{MeV/cm}\times Z_1\frac{\rho}{1\text{g/cc}}}{A_1\beta^2}\Big[f(\beta)+a_{\text{CM}}\Big] \tag{5}$$

where f_i is the atomic number fraction of ith element, $A_1 = \sum_i f_i A_i$, $Z_1 = \sum_i f_i Z_i$, and

$$a_{\text{CM}} = \frac{\sum_i Z_i f_i a_i}{Z_1} \tag{6}$$

where the subscript "CM" denotes "cold matter".

For the calculations of plasma stopping power, only electron contribution is considered, because the contribution of the plasma ions to stopping power is neglectable due to the fact that $m_i/m_e = 1836A \gg 1$. The expression of stopping power in plasma is simply the Bethe

ACCEPTED MANUSCRIPT
Review of Scientific Instruments
This is the author's peer reviewed, accepted manuscript. However, the online version of record will be different from this version once it has been copyedited and typeset.
PLEASE CITE THIS ARTICLE AS DOI:10.1063/1.5123392
AIP Publishing

formula under our assumptions in Eq(1) and (2)

$$\begin{aligned}\frac{d\langle E_p\rangle}{dx} &= -\frac{4\pi e^4 n_e}{\beta^2 m_e c^2}\ln\left[1.123\sqrt{\frac{1}{2\pi}}\frac{m_e^{3/2}c^2\beta^2/(1-\beta^2)}{\hbar e\sqrt{n_e}}\right] \\ &= -\frac{0.31\text{MeV/cm}\times Z\frac{\rho}{1\text{g/cc}}}{A\beta^2} \\ &\quad\times\Big[f(\beta)+10.2+0.5\ln A \\ &\quad -0.5\ln Z-0.5\ln(\frac{\rho}{1\text{g/cc}})\Big] \end{aligned} \tag{7}$$

where $\hbar$ is the reduced Planck constant. Eq (7) is consistent with the results from [53–55]. For the plasma composed of multiple ion species

$$\frac{d\langle E_p\rangle}{dx} = -\frac{0.31\text{MeV/cm}\times Z_1\frac{\rho}{1\text{g/cc}}}{A_1\beta^2}\Big[f(\beta)+a_{\text{Plasma}}\Big] \tag{8}$$

where A_1 and Z_1 has the same definitions as in the cold matter case but f_i's are replaced by the number fractions of ions. And

$$\begin{aligned}a_{\text{plasma}} &= \frac{\sum_i f_i Z_i\big(10.2+0.5\ln A_i-0.5\ln Z_i\big)}{Z_1} \\ &\quad -0.5\ln(\frac{\rho}{1\text{g/cc}})\end{aligned} \tag{9}$$

The difference between cold matter stopping power and plasma stopping power is only in the expressions for a_{CM} and a_{plasma}, i.e. Eq(6) and Eq(9), while other parts of the two equations are identical. The typical values of a_{CM} or a_{plasma} are around 10. In a typical HED target system, there are both cold matter and plasma. We use the ratio of Debye length λ_D to Fermi radius a_Z for quantifying the partition between cold matter and fully ionized plasma

$$\begin{aligned}\frac{\lambda_D}{a_Z} &= \frac{\sqrt{\frac{kT_e}{4\pi n_e^f e^2}}}{0.885a_0Z^{-1/3}} \\ &= \frac{0.5Z^{1/3}\sqrt{\frac{T}{1\text{eV}}}}{\sqrt{\frac{n_e^f}{10^{23}/\text{cc}}}}\end{aligned} \tag{10}$$

where a_0 is the Bohr radius and n_e^f is free electron density, i.e. not including the bond electrons, which is different from total electron density n_e, i.e. including both bond electrons and free electrons. For matter composed of multiple elements, we use logarithm averaged charge number $Z_{\text{lg}} = \exp(\sum_i f_i \log Z_i)$ in Eq(10). The total stopping power with combined cold matter and plasma is

$$(\frac{d\langle E_p\rangle}{dx})_{\text{total}} = -\frac{0.31\text{MeV/cm}\times Z_1\frac{\rho}{1\text{g/cc}}}{A_1\beta^2}\Big[f(\beta)+a_{\text{total}}\Big] \tag{11}$$

where

$$a_{\text{total}} = \frac{\lambda_D^2}{\lambda_D^2+a_Z^2}a_{\text{CM}} + \frac{a_Z^2}{\lambda_D^2+a_Z^2}a_{\text{plasma}} \tag{12}$$

The combination using Eq(12) is a good approximation if the transition layer between cold matter and plasma is thin compared to the fully cold matter or fully plasma regions, i.e. most regions in the modeling has $a_Z \ll \lambda_D$ or $a_Z \gg \lambda_D$. If $a_Z \approx \lambda_D$ dominates, then one need more precise combination model in the transition region. In Figure 1, we plot the ratio between the total stopping power with combined cold matter and plasma given by Eq(11) and cold matter approximation given by Eq(5) for plastic(CH with C:H=1) and copper, and for proton energy 14.7MeV and 3MeV. We use the mean ionization state from PROPACEOS[59] equation of state table to calculate the free electron density. The cold matter approximation is good for the matter near or above solid density, i.e. 1g/cc for CH and 8.9g/cc for Cu. For low densities, the correction from Eq(7) has significant contribution to total stopping power, especially for Cu. For high temperatures, i.e. $T > 50$eV, the correction from Eq(7) has larger contribution for CH than for Cu.

The straggling function of the proton energy, i.e. the variation of stopping power along the path of motion follows a Gaussian distribution[52]

$$F(\Delta,s) = \frac{1}{\sqrt{2\pi}\Omega}\exp[-\frac{(\Delta-\Delta_{\text{av}})^2}{2\Omega^2}] \tag{13}$$

with a variance Ω^2, and a mean value Δ_{av} equal to the product of path length s and the stopping power. The expression for the variance is[52, 56]

$$\begin{aligned}\Omega &= \sqrt{4\pi e^4 n_e\frac{1-\beta^2/2}{1-\beta^2}s} \\ &= 0.16\text{MeV}\sqrt{\frac{n_e}{10^{23}/\text{cc}}\frac{s}{1\text{cm}}\frac{1-\beta^2/2}{1-\beta^2}}\end{aligned} \tag{14}$$

which only depends on the electron density n_e, the path length s and the normalized velocity β of the proton.

In both Monte Carlo and ray-tracing calculations, three quantities are pre-calculated, (1) the coefficient for stopping power $\frac{0.31\text{MeV/cm}\times Z_1\frac{\rho}{1\text{g/cc}}}{A_1}$, (2) a_{total}, (3) $4\pi e^4 n_e$. In each time step of the particle motion, in both Monte Carlo and ray-tracing, the energy lost can be calculated from the pre-calculated quantities and the current value of β of the particle or ray, as given by Eq(11). In the Monte Carlo calculation, the straggling of proton energy is sampled at each time step using Eq(13). In the ray-tracing calculation, the total variable of proton energy is calculated by the numerical integration

$$\Omega^2_{\text{total}} = \sum_{\Delta s} 4\pi e^4 n_e\frac{1-\beta^2/2}{1-\beta^2}\Delta s \tag{15}$$

where the value of β is the current value for the particle and n_e is at the particle location.

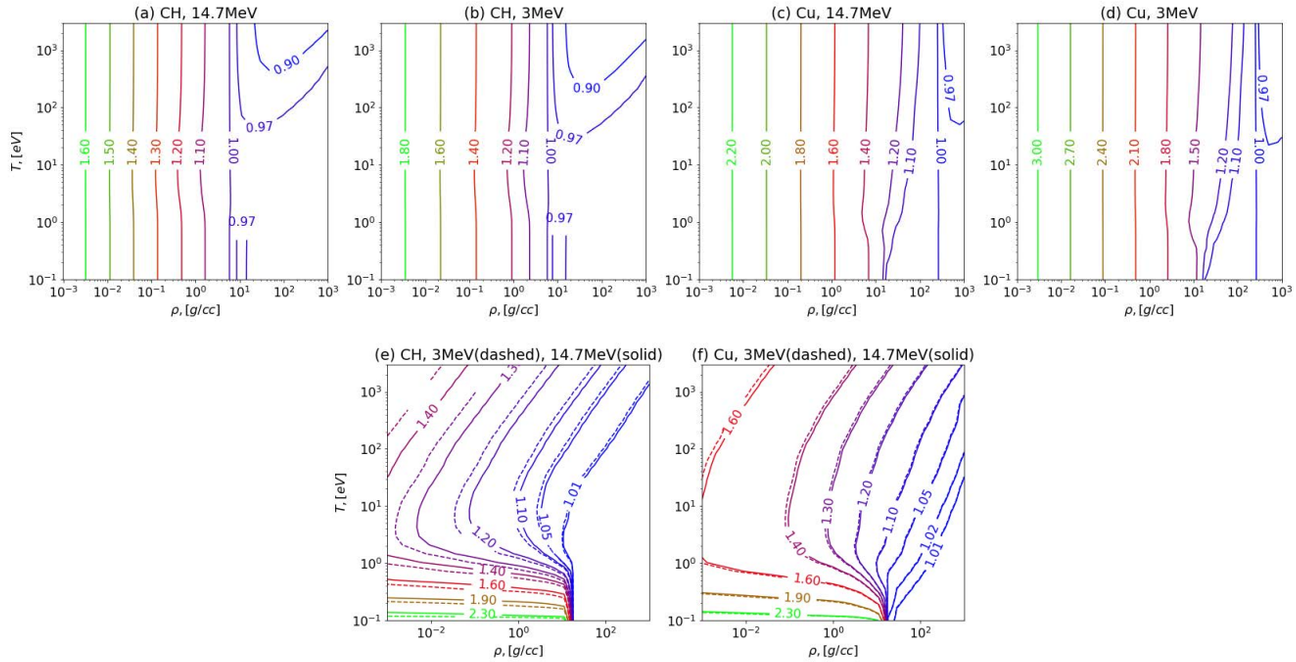

Figure 1. Subfigures (a) to (d) are the contours of the ratio between the total stopping power with the combined cold matter and plasma given by Eq(11) and cold matter approximation given by Eq(5), for four different cases: (a) plastic(C:H=1), proton energy $E = 14.7$MeV, (b) plastic(C:H=1), $E = 3.0$MeV, (c) copper, $E = 14.7$MeV, (d) copper, $E = 3$MeV. Subfigure (e) and (f) are the contours of the ratio between the scattering angle using the full characteristic small scattering angle given by Eq(20) and cold matter approximation, for four different case (e) CH with proton energy $E = 14.7$MeV and $E = 3$MeV, (f) Cu with proton energy $E = 14.7$MeV and $E = 3$MeV. There is slight difference between $E = 14.7$MeV and $E = 3$MeV. The column density is $\rho L = 0.005\text{g/cm}^2$ for (e) and (f). The horizontal axes of all the subfigures are densities, and the vertical axes of all the subfigures are electron temperatures.

B. Coulomb Scattering

The cross-section of single and multiple Coulomb scattering in thick foil was studied in [60, 61], which has been used in GEANT4[45] and MCNP[44]. The cross-section for large angle scattering remains unchanged from cold matter to plasma

$$Ns\sigma(\chi)\chi d\chi = 2\chi_c^2 \chi d\chi q(\chi)/\chi^4 \tag{16}$$

where $\sigma(\chi)\chi d\chi$ is the differential scattering cross section into the angular interval $d\chi$ by each atom(or ion), s is thickness of the material, N is the number of scattering atoms(or ions) per volume, q is the ratio of actual to Rutherford scattering and approaches unity for large angle scattering, and

$$\chi_c^2 = 4\pi N s e^4 Z(Z+1)/(pv)^2 \tag{17}$$

where p is the proton momentum and v the velocity of the proton beam. The physical meaning of χ_c, is that the total probability of single scattering through an angle greater than χ_c, is exactly one. For mixture, compound or isotopes

$$\chi_c^2 = 4\pi N s e^4 (Z_2^2 + Z_1)/(pv)^2 \tag{18}$$

where $Z_2 = \sqrt{\sum_i Z_i^2 f_i}$ and Z_1 is the same as that in Eq(6). The expression for the numerical value of χ_c^2 in terms of density ρ is

$$\chi_c^2 = 1.8 \times 10^{-7} \times \frac{\rho s}{\text{g/cm}^2} \frac{(Z_2^2 + Z_1)}{A} \frac{1-\beta^2}{\beta^4} \tag{19}$$

For Coulomb scattering in plasmas, we replace the Fermi radius a_Z of the atom with the Debye length λ_D of the plasma in the calculation of characteristic small scattering angle where $q(\chi)$ approaches zero. In general, for the regions with both cold matter and plasma, the characteristic small scattering angle is

$$\chi_0 = \lambda\!\!\!^{-} \sqrt{\frac{1}{a_Z^2} + \frac{1}{\lambda_D^2}} \tag{20}$$

where $\lambda\!\!\!^{-}$ is the De Broglie wavelength of the proton. For cold matter approximation, $\lambda_D/a_Z \to \infty$, Eq(20) recovers the characteristic small scattering angle in cold matter, which is identical to Eq(8) in Ref. [60].

For thick target where many scattering events occur, $B_c > 5$ for the variable B_c given by the following equations (we use B_c instead of B as in Ref. [60] to avoid

ACCEPTED MANUSCRIPT
Review of Scientific Instruments
This is the author's peer reviewed, accepted manuscript. However, the online version of record will be different from this version once it has been copyedited and typeset.
PLEASE CITE THIS ARTICLE AS DOI:10.1063/1.5123392
AIP Publishing

ACCEPTED MANUSCRIPT
Review of Scientific Instruments
This is the author's peer reviewed, accepted manuscript. However, the online version of record will be different from this version once it has been copyedited and typeset.
PLEASE CITE THIS ARTICLE AS DOI:10.1063/1.5123392
AIP Publishing

confusion with magnetic fields)

$$B_c - \ln B_c = b = \ln \frac{\chi_c^2}{1.167\chi_a^2} \tag{21}$$

$$\chi_a^2 = \chi_0^2\left(1.13 + 3.76(Z_2e^2)^2/(\hbar v)^2\right) \tag{22}$$

where $3.76(Z_2e^2)^2/(\hbar v)^2$ is the second order term in the Born approximation. In $\lambda_D/a_Z \to \infty$ limit, the expression for the numerical value of e^b without second order term in Born approximation is

$$e^b \approx \frac{6680\frac{\rho s}{\mathrm{g/cm^2}}(Z_2^2 + Z_1)}{\beta^2 A Z_{\mathrm{lg}}^{2/3}} \tag{23}$$

which is consistent with Eq(22) in Ref. [60]. The distribution of the scattering angle θ is expanded in a series of B_c. The tabulated numerical values of the distributions are in Ref. [60]. We keep the first three terms, i.e the Gaussian distribution (zeroth order term) with

$$\sigma_{\mathrm{Gauss}} = \chi_c(B_c/2)^{1/2} \tag{24}$$

and the terms in $\frac{1}{B_c}$ and $\frac{1}{B_c^2}$. The distribution is closer to Gaussian distribution when B_c becomes larger. At each time step of proton motion, B_c is calculated, using the length step Δs as the target thickness s in Eq(18). In Monte Carlo calculation, if B_c if small, i.e $B_c < 5$, we fallback to use the cross section for single scattering. The method we implement for Coulomb scattering as a random process has been used in other Monte Carlo codes such as MCNP[62] and GEANT4[45]. Two quantities in each cell are pre-calculated before the Monte Carlo or ray-tracing calculations. (1) the coefficient for large angle scattering cross section, i.e. $4\pi N e^4(Z_2^2+Z_1)$, where $Z_2 = \sqrt{\sum_i Z_i^2 f_i}$, (2) the characteristic small scattering angle χ_0.

For ray tracing calculation, we use the numerical integration of the R.H.S. of Eq(18) and the ion+atom density weighted value of $\ln \chi_0$

$$\ln \chi_0 = \frac{\sum_{\Delta s}(N \ln \chi_0)\big|_{\mathrm{local}} \Delta s}{\sum_{\Delta s} N\big|_{\mathrm{local}} \Delta s} \tag{25}$$

which is an analog of Eq(16) in Ref. [60]. In Figure 1(e) and (f), we show the ratio between the scattering angle using the full characteristic small scattering angle given by Eq(20) and using cold matter approximation. The scattering angle is calculated using Eq(24), and B_c, χ_c are calculated by ray-tracing of proton beam through a material with column density is $\rho L = 0.005\mathrm{g/cm^2}$. For low densities or high temperatures, the correction from finite λ_D has significant contribution to total scattering angle as shown in the top left corner of Figure 1(e) and (f). The difference between 3MeV and 14.7MeV protons is more prominent in CH than in Cu, which can be explained by the sensitivity of b to the proton energy or proton velocity given Eq(21) and Eq(22). For CH, $3.76(Z_2e^2)^2/(\hbar v)^2$ is 0.6 for $E_p = 3$MeV and 0.1 for $E_p = 14.7$MeV, both less than 1.13, thus $e^b \sim \frac{1}{v^2(1.13+3.76(Z_2e^2)^2/(\hbar v)^2)}$ is sensitive to proton energy. For Cu, $3.76(Z_2e^2)^2/(\hbar v)^2$ is 26 for $E_p = 3$MeV and 5 for $E_p = 14.7$MeV, both much larger than 1.13, thus $e^b \sim \frac{1}{v^2(1.13+3.76(Z_2e^2)^2/(\hbar v)^2)} \sim \frac{1}{v^2\times 3.76(Z_2e^2)^2/(\hbar v)^2} \sim$ constant.

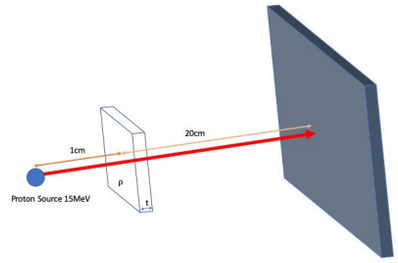

Figure 2. Illustration of simulation setup for the benchmark of MPRAD against MCNP and also for the example applications. The distance from the proton source to the body center plane of the matter is 1cm. The density of the matter is ρ and the thickness is t. The detector plane is parallel to the slab of matter and is 20cm away from the the body center plane of the cold matter. The detector size is 2cm × 2cm.

III. BENCHMARK AGAINST MCNP CODE FOR COLD MATTER

Under cold matter approximation, we test the Monte Carlo calculation in MPRAD code by the setup as shown in Fig 2. The mono-energetic($\Delta E_p = 0$) and collimated proton source with $E_p = 15$MeV is placed 1cm from the slab of matter with given material and thickness. We use 10^6 particles in the simulations and the proton velocity is perpendicular to the detector plane. The detector plane is 20cm from the slab of matter, and the particles reaching the detector plane are binned by spacial grid with $\Delta x = \Delta y = 0.01$cm and energy grid with $\Delta E = 0.05$MeV. The simulation with the same setup is also carried out using MCNP code[44].

For all the test cases, both the spatially binned proton image and the proton spectrum are consistent between MPRAD and MCNP. An example is shown in Fig 3. The protons in the narrow beam are isotropically scattered by colliding with the matter in the slab, so a circular spot on the detector plane is produced as shown in Fig 3(b) and (c). The protons lose energy and have a finite width in the spectrum at the detector as shown in Fig 3(a), because different protons have different path length in the matter due to scattering. For a given composition of the slab material, different density ρ but same column density ρt produces similar image and spectrum. Quantitative comparison between the results from MPRAD and MCNP is shown in Table I and Table II. The slight difference between results from MPRAD and MCNP is tolerant for typical proton radiography setup in HED ex-

ACCEPTED MANUSCRIPT
Review of Scientific Instruments
This is the author's peer reviewed, accepted manuscript. However, the online version of record will be different from this version once it has been copyedited and typeset.
PLEASE CITE THIS ARTICLE AS DOI:10.1063/1.5123392
AIP Publishing

periments, where the spectrum width of the source is a few keV to MeV[2, 40, 48].

IV. EXAMPLE APPLICATIONS

For small angle deflection, the deflection angle of protons by magnetic field is [43]

$$\alpha = 1.80\times10^{-2}\text{rad}\times\big(\frac{E_p}{14.7\text{MeV}}\big)^{-1/2} \times\big(\frac{B}{10^5\text{G}}\big)\times\big(\frac{l_i}{0.1\text{cm}}\big) \tag{26}$$

where E_p is the energy of proton, B is the strength of magnetic field, and l_i is the longitudinal size of the interaction region. From Eq(24) and Eq(26) we can calculate the ratio between the deflection angle by magnetic field and the Coulomb scattering angle

$$\begin{aligned}\frac{\alpha}{\sigma_{\text{Gauss}}} &= \frac{2\sqrt{A}}{\sqrt{B_c(Z_2^2+Z_1)}}\sqrt{\frac{E_p}{m_pc^2}}\frac{v_A}{c}\sqrt{\frac{l_im_pc^2}{e^2}}\\ &= \frac{6\sqrt{A}}{\sqrt{B_c(Z_2^2+Z_1)}}\big(\frac{E_p}{14.7\text{MeV}}\big)^{1/2} \times\frac{v_A}{2.8\times10^4\text{cm/s}}\big(\frac{l_i}{0.1\text{cm}}\big)\end{aligned} \tag{27}$$

where v_A is the Alfvén speed, i.e. $v_A=\frac{B}{\sqrt{4\pi\rho}}$.

For the examples we show in this Section, we use the setup as shown in Figure 2, with a magnetic field in the slab. We carry out Monte Carlo runs with a flux rope of toroidal fields, a flux rope of poloidal fields, and a turbulent field that satisfies the power law energy spectrum. The z axis is along the line of sight, and the detector plane is $x-y$ plane. The interaction region is filled with plastic(C:H=1). The thickness of the interaction region is $l_i=1000\mu$m with uniform tunable density ρ and fixed temperature $T_e=100$eV. And the field is centered at $(0,0,0)$. The source is at $(0,0,-1\text{cm})$, mono-energetic and collimated with $E_p=15$MeV.

We use the same notation from Ref. [43] to define the contrast field

$$\Lambda(\boldsymbol{x}_\perp)=\frac{\Psi(\boldsymbol{x}_\perp)-\psi_0}{\psi_0} \tag{28}$$

where ψ_0 is the unperturbed proton flux, which is uniform by assumption, $\Psi(\boldsymbol{x}_\perp)$ is the perturbed proton flux by both deflection and diffusion, and $\boldsymbol{x}_\perp$ is the position vector on the image plane. Eq(19) in Ref. [43] gives the expression for the contrast field as a map of MHD current

$$\Lambda(\boldsymbol{x}_\perp)=\frac{er_i(r_s-r_i)}{r_s\sqrt{2m_pc^2E_p}}\hat{z}\cdot\int dz\ \nabla\times\boldsymbol{B} \tag{29}$$

where r_s is the distance between the interaction region and the screen, r_i is the distance between the source and the image plate. For the parameters we use, we have

$$\Lambda(\boldsymbol{x}_\perp)=1.7\times10^{-6}\text{G}^{-1}\times\big(\frac{E_p}{14.7\text{MeV}}\big)^{-1/2} \times\hat{z}\cdot\int dz\ \nabla\times\boldsymbol{B} \tag{30}$$

We use the field strength that makes $|\Lambda(\boldsymbol{x}_\perp)|<1$ to avoid caustics.

A. Localized magnetic fields

Toroidal magnetic fields have been observed and measured in some HED experiments[1, 13–18, 20–22, 34, 35], especially for the reconnection geometry. The typical geometry of self-generated magnetic field in the plasma plume produced by single laser spot is toroidal. We follow the expression for toroidal magnetic field in literatures[41, 43, 47], which is the characteristic distribution of a localized toroidal field

$$\overrightarrow{B}=\frac{B_0}{a}\exp(-\frac{x^2+y^2+z^2}{a^2})(-y,x,0) \tag{31}$$

where we use $B_0=1\times10^5$G, $a=200\mu$m for our numerical tests.

As shown in Figure 4(a), the quasi-monoenergetic proton beam has become a beam with a broad energy distribution as it goes through the target region, and the mean energy becomes lower than the source energy. In the analysis for real data from the experiments, one also has to take the spectrum width of the source into account. The diffusion can affect the interpretation of proton image. As the density increases, the theoretical peak value of the contrast drops as $E_p^{-1/2}$ given by Eq(30) if no diffusion is considered. However, the peak value of the contrast in the simulation drops faster than the theoretical value given by Eq(30), as shown in Figure 4(c). One deduces smaller field or MHD current from the image for large density case. For large densities, the variation level of proton number in each pixel can potentially become comparable or even smaller than the poisson noise for the CR-39 image, and the variation level of the proton flux can become smaller than the sensitivity of radiochromic film.

A few HED experiments have generated and characterized poloidal magnetic field, such as supersonic jets with mega-gauss self-generated magnetic fields localized in the interaction region[24, 25]. We follow the expression for poloidal magnetic field in literatures[41, 47], which is the characteristic distribution of a localized poloidal field

$$B_y=B_0\exp(-\frac{x^2+z^2}{a^2}) \tag{32}$$

where we use $B_0=4\times10^5$G, $a=200\mu$m for our numerical tests. The results are shown in Figure 4(d) and (e). Similar to the case for the toroidal magnetic fields, the

ACCEPTED MANUSCRIPT
Review of Scientific Instruments
This is the author's peer reviewed, accepted manuscript. However, the online version of record will be different from this version once it has been copyedited and typeset.
PLEASE CITE THIS ARTICLE AS DOI:10.1063/1.5123392
AIP Publishing

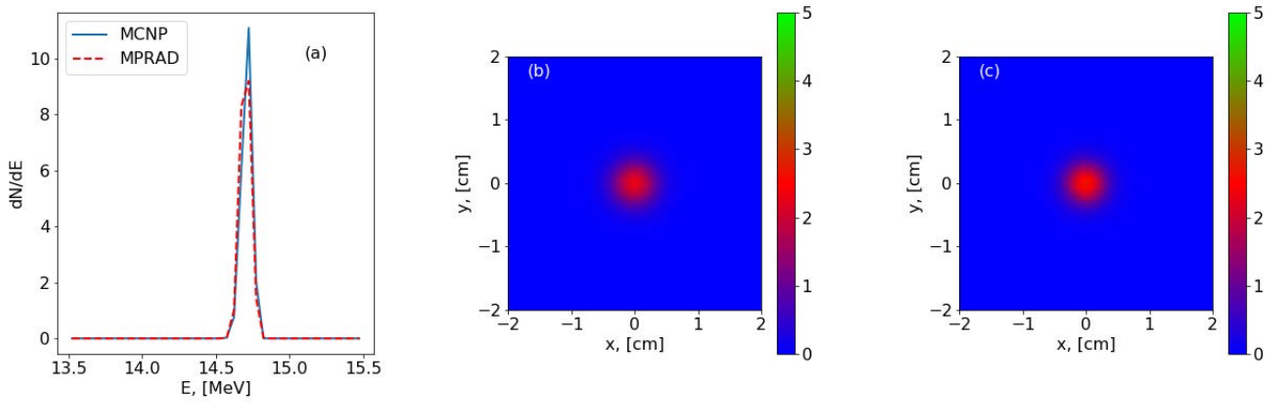

Figure 3. Results of proton radiography simulation for a slab of 8.96g/cc and 16μm copper. (a) The energy grid is $\Delta E = 0.05$MeV. The unit of the vertical axis is (number of particles)/MeV normalized by total particle number $N = 10^6$. The red dash curve is for MPRAD, the solid blue curve is for MCNP. (b) The image generated using MPRAD, the spatial grid is $\Delta x = \Delta y = 0.01$cm. (c) same as (b) but using MCNP. The unit of the color code is (number of particles)/cm^2 normalized by total particle number $N = 10^6$.

Table I. Comparison of average energy and energy variation from MPRAD and MCNP for different material, density and thickness

Material, density, thickness	$\overline{E}$(MeV), MPRAD	$\overline{E}$(MeV), MCNP	$\sqrt{\overline{E^2}-\overline{E}^2}$(MeV), MPRAD	$\sqrt{\overline{E^2}-\overline{E}^2}$(MeV), MCNP
Be, 1.85g/cc, 200μm	13.96	13.96	0.0546	0.0565
Be, 7.40g/cc, 50μm	13.96	13.96	0.0546	0.0565
Mg, 1.74g/cc, 16μm	14.93	14.92	0.0157	0.0138
Mg, 6.96g/cc, 4μm	14.93	14.92	0.0157	0.0138
Cu, 8.96g/cc, 16μm	14.70	14.71	0.0355	0.0350
Cu, 17.92g/cc, 8μm	14.70	14.71	0.0355	0.0350

diffusion of the beam affect the final spectrum of the protons and the peak value of proton flux contrast, and thus some care are needed for interpreting the proton images.

B. Power law energy spectrum in magnetic turbulence

Magnetic turbulence and dynamo have been studied in HED experiments[37, 38]. In turbulent magnetic fields, magnetic energy cascades to small scales, and the magnetic energy spectrum follows a power law distribution. The power law spectrum can be inferred using inverse-problem type of technique[37, 38, 43]. As an example for using MPRAD to study how diffusion affect the inferred spectrum, we use a power law in a recently designed turbulent dynamo experiment on the OMEGA-EP[63], where the magnetic energy spectrum follows $E(k) \propto k^{-2.3}$. The method for generating the magnetic field by random numbers for numerical tests is discussed in Ref. [42], and the vector potential is multiplied by $\exp(-\frac{x^2+y^2+z^2}{a^2})$ where $a = 200\mu$m to get the localized field. We assume the RMS value of the magnetic field in the l_i^3 box is $B_{\rm rms} = 1\times10^4$G, the maximum field strength is $B_{\rm max} = 1\times10^5$G, the same as the test problem for localized toroidal and poloidal magnetic fields. We use the algorithm in Ref. [43] to reconstruct the divergence free turbulence spectrum. For reconstruction, Eq(52) in Ref. [43] gives the expression for the inferred magnetic energy density

$$E_B(\frac{r_s}{r_i}\frac{2\pi}{L}|\boldsymbol{n}|) = \frac{2\pi}{e^2(r_s-r_i)^2 l_i L^2}\langle\hat{\Lambda}(\boldsymbol{n})\hat{\Lambda}(\boldsymbol{n})^*\rangle \qquad (33)$$

where l_i is the longitudinal size of the interaction region, L is the length and width of the image plate, $\hat{\Lambda}(\boldsymbol{n})$ is the discretized Fourier transform of $\Lambda(\boldsymbol{x}_\perp)$, and the average is over cells in $\boldsymbol{n}$-space for the discretized Fourier transform.

As shown in Figure 4(f), the diffusion affects the cutoff length scale π/k_c of the spectrum given by the inversion algorithm. The results for $\rho = 10^{-7}$g/cc shows little scattering and the spectrum around $k \sim 10^3$cm^{-1} agrees being a the power law, and $k > 3\times10^3$cm^{-1} is beyond the resolution limit. For densities from $\rho = 3.0\times10^{-4}$ and above, there is a critical wavevector k_c that the diffusion affect damps the small scale feature for $k > k_c$ but retains the large scale feature for $k < k_c$. For $\rho = 7.3\times10^{-3}$g/cc

ACCEPTED MANUSCRIPT
Review of Scientific Instruments
This is the author's peer reviewed, accepted manuscript. However, the online version of record will be different from this version once it has been copyedited and typeset.
PLEASE CITE THIS ARTICLE AS DOI:10.1063/1.5123392
AIP Publishing

Table II. Comparison of weighted(by proton flux) average of x^2+y^2 from MPRAD and MCNP for different material, density and thickness

Material, density, thickness	$\sqrt{\overline{x^2+y^2}}$(cm), MPRAD	$\sqrt{\overline{x^2+y^2}}$(cm), MCNP
Be, 1.85g/cc, 200μm	0.381	0.369
Be, 7.40g/cc, 50μm	0.381	0.369
Mg, 1.74g/cc, 16μm	0.161	0.161
Mg, 6.96g/cc, 4μm	0.161	0.161
Cu, 8.96g/cc, 16μm	0.535	0.536
Cu, 17.92g/cc, 8μm	0.535	0.536

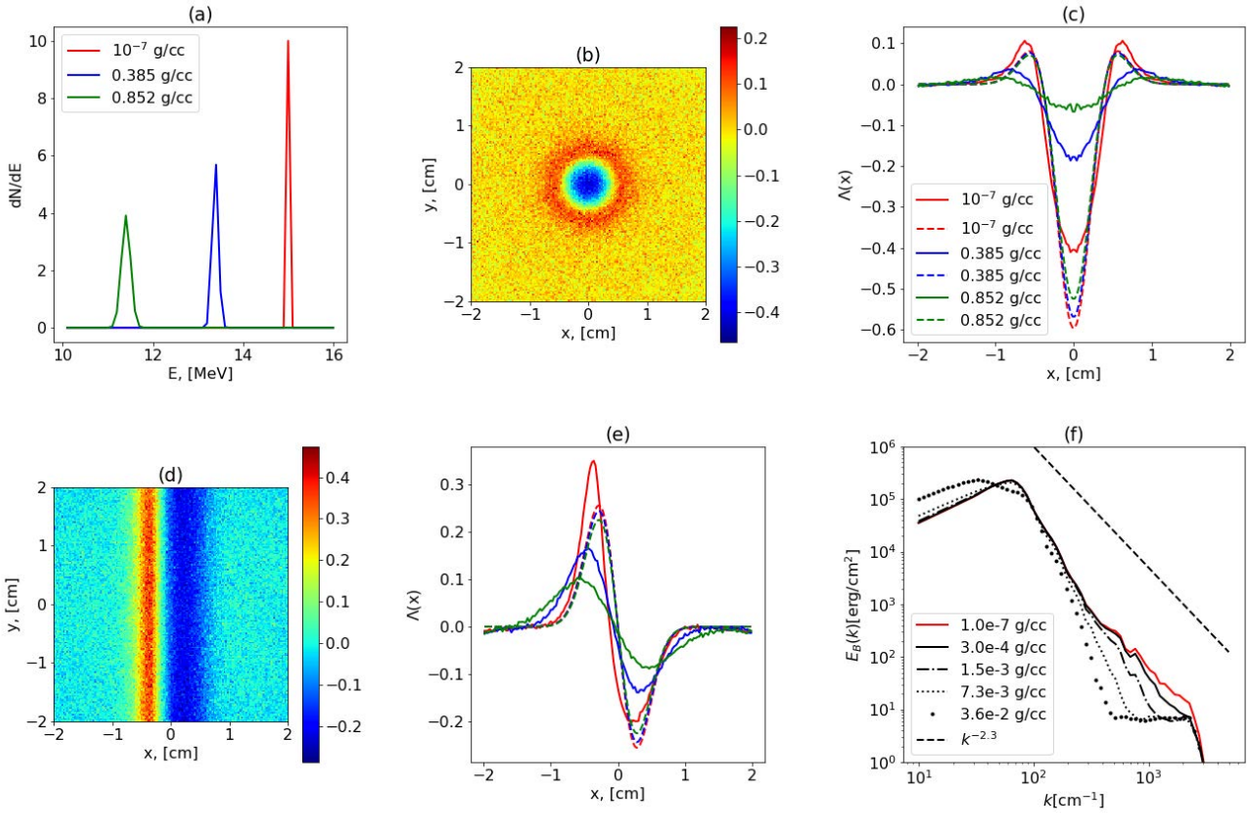

Figure 4. The results for the example applications for 1000μm thickness. The colors of the curves are consistent among all panels, red for $\rho = 10^{-7}$g/cc, blue for $\rho = 0.385$g/cc, green for $\rho = 0.852$g/cc, and black otherwise. Subfigure (a) shows the spectrum of the protons in the detector plane for different densities. Subfigure (b) is the contrast field of the proton image for the test case for localized toroidal magnetic field, the feature is coaxial as we can see from the symmetry of the field. A line-out cross the center is shown in (c), for different densities. The dashed lines are the theoretical value of contrast given by Eq(30), and the solid lines are from the MPRAD simulations. The results for the localized poloidal magnetic field is in (d) and (e). Subfigure (f) is the inferred turbulence magnetic energy spectrum using Eq(33), for different densities.

and $\rho = 3.6\times10^{-2}$g/cc, the energy density at low k, i.e. $k < 50\text{cm}^{-1}$ becomes higher than other densities. The inverse of the cutoff scale k_c is roughly the scattering angle multiplied by r_i, thus

$$k_c \approx \frac{\pi}{10 r_i \sigma_{\text{Gauss}}} \approx 20\text{cm}^{-1}\left(\frac{\rho}{1\text{g/cc}}\right)^{-1/2} \quad (34)$$

where the factor 10 in the denominator is an estimate of the scattering angle in $\frac{1}{B_c}$ term. B_c is roughly 6 for $\rho = 1.5\times10^{-3}$g/cc so that $\frac{1}{B_c}$ term is not neglectable.

ACCEPTED MANUSCRIPT
Review of Scientific Instruments
This is the author's peer reviewed, accepted manuscript. However, the online version of record will be different from this version once it has been copyedited and typeset.
PLEASE CITE THIS ARTICLE AS DOI:10.1063/1.5123392
AIP Publishing

The estimate for k_c is in good agreement with the results in Figure4(f). In the analysis for real data from the experiments, one also has to take the angular distribution of the source into account. The composition and temperature can also affect k_c.

V. SUMMARY

A simulation tool MPRAD is developed in this work, which extends the capability of Monte Carlo calculations for proton radiography, especially for the conditions where Coulomb scattering and stopping power are not neglectable. The model for Coulomb scattering and stopping power in fully ionized plasma and in cold matter are combined to improve the accuracy of modeling, especially in the plasma region. Ray tracing can be used as a quick way to study the effects of Coulomb scattering and stopping power. Synthetic Monte Carlo radiograph by using the imported data of fields, density, mass fraction and temperature distribution from plasma-dynamical modeling can be useful for studying the interplay between the effect from density and from electromagnetic fields. Such kind of synthetic radiograph can aid optimizing the designs for experiments, especially for the platforms where obstacle or high density plasma is unavoidable.

TNSA protons with high energy are better to make the $\alpha/\sigma_{\text{Gauss}}$ larger as given by Eq(27), thus the deflection by electromagnetic fields is more prominent than the diffusion of the beam. The proton beam from fusion source can still be useful for the magnetic field measurement, although the dynamical range is affected by the diffusion. The signal on the proton image appears in a wide range of energy band instead of a narrow band as the original beam, which potentially gives us more information about the magnetic fields for reconstructing field structure. However, obtaining the proton images for different energy bands put challenges on the etching process of CR-39[39]. The Monte Carlo simulations with scattering and energy lost included are needed for optimizing the etching process.

VI. ACKNOWLEDGEMENTS

YL is grateful to Alex Zylstra, Hong Sio, Andrew Birkel, Sky Sjue, Mario Manuel, Don Lamb, Petros Tzeferacos and Matthew Baring for valuable discussions. Research presented in this paper was supported by the Laboratory Directed Research and Development(LDRD) program of Los Alamos National Laboratory(LANL). The simulations were performed with LANL Institutional Computing which is supported by the U.S. Department of Energy National Nuclear Security Administration under Contract No. 89233218CNA000001, and with the Extreme Science and Engineering Discovery Environment (XSEDE), which is supported by National Science Foundation(NSF) grant number ACI-1548562.

[1] C. K. Li, F. H. Séguin, J. A. Frenje, J. R. Rygg, R. D. Petrasso, R. P. J. Town, P. A. Amendt, S. P. Hatchett, O. L. Landen, A. J. Mackinnon, P. K. Patel, V. A. Smalyuk, T. C. Sangster, and J. P. Knauer, Physical Review Letters **97** (2006), 10.1103/physrevlett.97.135003.

[2] A. B. Zylstra, C. K. Li, H. G. Rinderknecht, F. H. Séguin, R. D. Petrasso, C. Stoeckl, D. D. Meyerhofer, P. Nilson, T. C. Sangster, S. L. Pape, A. Mackinnon, and P. Patel, Review of Scientific Instruments **83**, 013511 (2012).

[3] J. R. Rygg, F. H. Seguin, C. K. Li, J. A. Frenje, M. J.-E. Manuel, R. D. Petrasso, R. Betti, J. A. Delettrez, O. V. Gotchev, J. P. Knauer, D. D. Meyerhofer, F. J. Marshall, C. Stoeckl, and W. Theobald, Science **319**, 1223 (2008).

[4] C. K. Li, F. H. Séguin, J. R. Rygg, J. A. Frenje, M. Manuel, R. D. Petrasso, R. Betti, J. Delettrez, J. P. Knauer, F. Marshall, D. D. Meyerhofer, D. Shvarts, V. A. Smalyuk, C. Stoeckl, O. L. Landen, R. P. J. Town, C. A. Back, and J. D. Kilkenny, Physical Review Letters **100** (2008), 10.1103/physrevlett.100.225001.

[5] C. K. Li, F. H. Séguin, J. A. Frenje, R. D. Petrasso, P. A. Amendt, R. P. J. Town, O. L. Landen, J. R. Rygg, R. Betti, J. P. Knauer, D. D. Meyerhofer, J. M. Soures, C. A. Back, J. D. Kilkenny, and A. Nikroo, Physical Review Letters **102** (2009), 10.1103/physrevlett.102.205001.

[6] C. K. Li, F. H. Seguin, J. A. Frenje, M. Rosenberg, R. D. Petrasso, P. A. Amendt, J. A. Koch, O. L. Landen, H. S. Park, H. F. Robey, R. P. J. Town, A. Casner, F. Philippe, R. Betti, J. P. Knauer, D. D. Meyerhofer, C. A. Back, J. D. Kilkenny, and A. Nikroo, Science **327**, 1231 (2010).

[7] C. K. Li, F. H. Séguin, J. A. Frenje, M. J. Rosenberg, H. G. Rinderknecht, A. B. Zylstra, R. D. Petrasso, P. A. Amendt, O. L. Landen, A. J. Mackinnon, R. P. J. Town, S. C. Wilks, R. Betti, D. D. Meyerhofer, J. M. Soures, J. Hund, J. D. Kilkenny, and A. Nikroo, Physical Review Letters **108** (2012), 10.1103/physrevlett.108.025001.

[8] F. H. Séguin, C. K. Li, M. J.-E. Manuel, H. G. Rinderknecht, N. Sinenian, J. A. Frenje, J. R. Rygg, D. G. Hicks, R. D. Petrasso, J. Delettrez, R. Betti, F. J. Marshall, and V. A. Smalyuk, Physics of Plasmas **19**, 012701 (2012).

[9] I. V. Igumenshchev, A. B. Zylstra, C. K. Li, P. M. Nilson, V. N. Goncharov, and R. D. Petrasso, Physics of Plasmas **21**, 062707 (2014).

[10] A. J. Mackinnon, P. K. Patel, M. Borghesi, R. C. Clarke, R. R. Freeman, H. Habara, S. P. Hatchett, D. Hey, D. G. Hicks, S. Kar, M. H. Key, J. A. King, K. Lancaster, D. Neely, A. Nikkro, P. A. Norreys, M. M. Notley, T. W. Phillips, L. Romagnani, R. A. Snavely, R. B. Stephens, and R. P. J. Town, Physical Review Letters **97** (2006), 10.1103/physrevlett.97.045001.

[11] L. Volpe, D. Batani, B. Vauzour, P. Nicolai, J. J. Santos, C. Regan, A. Morace, F. Dorchies, C. Fourment, S. Hulin, F. Perez, S. Baton, K. Lancaster, M. Galimberti, R. Heathcote, M. Tolley, C. Spindloe, P. Koester, L. Labate, L. A. Gizzi, C. Benedetti, A. Sgattoni,

ACCEPTED MANUSCRIPT
Review of Scientific Instruments
This is the author's peer reviewed, accepted manuscript. However, the online version of record will be different from this version once it has been copyedited and typeset.
PLEASE CITE THIS ARTICLE AS DOI:10.1063/1.5123392
AIP Publishing

M. Richetta, J. Pasley, F. Beg, S. Chawla, D. P. Higginson, and A. G. MacPhee, Physics of Plasmas **18**, 012704 (2011).

[12] F. Perez, M. Koenig, D. Batani, S. D. Baton, F. N. Beg, C. Benedetti, E. Brambrink, S. Chawla, F. Dorchies, C. Fourment, M. Galimberti, L. A. Gizzi, R. Heathcote, D. P. Higginson, S. Hulin, R. Jafer, P. Koester, L. Labate, K. Lancaster, A. J. MacKinnon, A. G. McPhee, W. Nazarov, P. Nicolai, J. Pasley, A. Ravasio, M. Richetta, J. J. Santos, A. Sgattoni, C. Spindloe, B. Vauzour, and L. Volpe, Plasma Physics and Controlled Fusion **51**, 124035 (2009).

[13] C. K. Li, F. H. Séguin, J. A. Frenje, J. R. Rygg, R. D. Petrasso, R. P. J. Town, O. L. Landen, J. P. Knauer, and V. A. Smalyuk, Physical Review Letters **99** (2007), 10.1103/physrevlett.99.055001.

[14] P. M. Nilson, L. Willingale, M. C. Kaluza, C. Kamperidis, S. Minardi, M. S. Wei, P. Fernandes, M. Notley, S. Bandyopadhyay, M. Sherlock, R. J. Kingham, M. Tatarakis, Z. Najmudin, W. Rozmus, R. G. Evans, M. G. Haines, A. E. Dangor, and K. Krushelnick, Physics of Plasmas **15**, 092701 (2008).

[15] L. Willingale, P. M. Nilson, M. C. Kaluza, A. E. Dangor, R. G. Evans, P. Fernandes, M. G. Haines, C. Kamperidis, R. J. Kingham, C. P. Ridgers, M. Sherlock, A. G. R. Thomas, M. S. Wei, Z. Najmudin, K. Krushelnick, S. Bandyopadhyay, M. Notley, S. Minardi, M. Tatarakis, and W. Rozmus, Physics of Plasmas **17**, 043104 (2010).

[16] G. Fiksel, W. Fox, A. Bhattacharjee, D. Barnak, P.-Y. Chang, K. Germaschewski, S. Hu, and P. Nilson, Physical Review Letters **113** (2014), 10.1103/physrevlett.113.105003.

[17] M. Rosenberg, C. Li, W. Fox, I. Igumenshchev, F. Séguin, R. Town, J. Frenje, C. Stoeckl, V. Glebov, and R. Petrasso, Nature Communications **6** (2015), 10.1038/ncomms7190.

[18] M. Rosenberg, C. Li, W. Fox, A. Zylstra, C. Stoeckl, F. Séguin, J. Frenje, and R. Petrasso, Physical Review Letters **114** (2015), 10.1103/physrevlett.114.205004.

[19] C. K. Li, F. H. Séguin, J. A. Frenje, J. R. Rygg, R. D. Petrasso, R. P. J. Town, P. A. Amendt, S. P. Hatchett, O. L. Landen, A. J. Mackinnon, P. K. Patel, M. Tabak, J. P. Knauer, T. C. Sangster, and V. A. Smalyuk, Physical Review Letters **99** (2007), 10.1103/physrevlett.99.015001.

[20] C. A. Cecchetti, M. Borghesi, J. Fuchs, G. Schurtz, S. Kar, A. Macchi, L. Romagnani, P. A. Wilson, P. Antici, R. Jung, J. Osterholtz, C. A. Pipahl, O. Willi, A. Schiavi, M. Notley, and D. Neely, Physics of Plasmas **16**, 043102 (2009).

[21] R. D. Petrasso, C. K. Li, F. H. Seguin, J. R. Rygg, J. A. Frenje, R. Betti, J. P. Knauer, D. D. Meyerhofer, P. A. Amendt, D. H. Froula, O. L. Landen, P. K. Patel, J. S. Ross, and R. P. J. Town, Physical Review Letters **103** (2009), 10.1103/physrevlett.103.085001.

[22] C. K. Li, F. H. Séguin, J. A. Frenje, M. Manuel, D. Casey, N. Sinenian, R. D. Petrasso, P. A. Amendt, O. L. Landen, J. R. Rygg, R. P. J. Town, R. Betti, J. Delettrez, J. P. Knauer, F. Marshall, D. D. Meyerhofer, T. C. Sangster, D. Shvarts, V. A. Smalyuk, J. M. Soures, C. A. Back, J. D. Kilkenny, and A. Nikroo, Physics of Plasmas **16**, 056304 (2009).

[23] C. K. Li, D. D. Ryutov, S. X. Hu, M. J. Rosenberg, A. B. Zylstra, F. H. Séguin, J. A. Frenje, D. T. Casey, M. G. Johnson, M. J.-E. Manuel, H. G. Rinderknecht, R. D. Petrasso, P. A. Amendt, H. S. Park, B. A. Remington, S. C. Wilks, R. Betti, D. H. Froula, J. P. Knauer, D. D. Meyerhofer, R. P. Drake, C. C. Kuranz, R. Young, and M. Koenig, Physical Review Letters **111** (2013), 10.1103/physrevlett.111.235003.

[24] L. Gao, E. Liang, Y. Lu, R. K. Follet, H. Sio, P. Tzeferacos, D. H. Froula, A. Birkel, C. K. Li, D. Lamb, R. Petrasso, W. Fu, M. Wei, and H. Ji, The Astrophysical Journal **873**, L11 (2019).

[25] Y. Lu, P. Tzeferacos, E. Liang, R. K. Follett, L. Gao, A. Birkel, D. H. Froula, W. Fu, H. Ji, D. Lamb, C. K. Li, H. Sio, R. Petrasso, and M. S. Wei, Physics of Plasmas **26**, 022902 (2019).

[26] M. J.-E. Manuel, C. K. Li, F. H. Séguin, J. Frenje, D. T. Casey, R. D. Petrasso, S. X. Hu, R. Betti, J. D. Hager, D. D. Meyerhofer, and V. A. Smalyuk, Physical Review Letters **108** (2012), 10.1103/physrevlett.108.255006.

[27] L. Gao, P. M. Nilson, I. V. Igumenschev, S. X. Hu, J. R. Davies, C. Stoeckl, M. G. Haines, D. H. Froula, R. Betti, and D. D. Meyerhofer, Physical Review Letters **109** (2012), 10.1103/physrevlett.109.115001.

[28] N. L. Kugland, J. S. Ross, P.-Y. Chang, R. P. Drake, G. Fiksel, D. H. Froula, S. H. Glenzer, G. Gregori, M. Grosskopf, C. Huntington, M. Koenig, Y. Kuramitsu, C. Kuranz, M. C. Levy, E. Liang, D. Martinez, J. Meinecke, F. Miniati, T. Morita, A. Pelka, C. Plechaty, R. Presura, A. Ravasio, B. A. Remington, B. Reville, D. D. Ryutov, Y. Sakawa, A. Spitkovsky, H. Takabe, and H.-S. Park, Physics of Plasmas **20**, 056313 (2013).

[29] W. Fox, G. Fiksel, A. Bhattacharjee, P.-Y. Chang, K. Germaschewski, S. X. Hu, and P. M. Nilson, Physical Review Letters **111** (2013), 10.1103/physrevlett.111.225002.

[30] M. J.-E. Manuel, C. K. Li, F. H. Séguin, N. Sinenian, J. A. Frenje, D. T. Casey, R. D. Petrasso, J. D. Hager, R. Betti, S. X. Hu, J. Delettrez, and D. D. Meyerhofer, Physics of Plasmas **20**, 056301 (2013).

[31] L. Gao, P. M. Nilson, I. V. Igumenschev, G. Fiksel, R. Yan, J. R. Davies, D. Martinez, V. Smalyuk, M. G. Haines, E. G. Blackman, D. H. Froula, R. Betti, and D. D. Meyerhofer, Physical Review Letters **110** (2013), 10.1103/physrevlett.110.185003.

[32] H.-S. Park, C. M. Huntington, F. Fiuza, R. P. Drake, D. H. Froula, G. Gregori, M. Koenig, N. L. Kugland, C. C. Kuranz, D. Q. Lamb, M. C. Levy, C. K. Li, J. Meinecke, T. Morita, R. D. Petrasso, B. B. Pollock, B. A. Remington, H. G. Rinderknecht, M. Rosenberg, J. S. Ross, D. D. Ryutov, Y. Sakawa, A. Spitkovsky, H. Takabe, D. P. Turnbull, P. Tzeferacos, S. V. Weber, and A. B. Zylstra, Physics of Plasmas **22**, 056311 (2015).

[33] C. M. Huntington, F. Fiuza, J. S. Ross, A. B. Zylstra, R. P. Drake, D. H. Froula, G. Gregori, N. L. Kugland, C. C. Kuranz, M. C. Levy, C. K. Li, J. Meinecke, T. Morita, R. Petrasso, C. Plechaty, B. A. Remington, D. D. Ryutov, Y. Sakawa, A. Spitkovsky, H. Takabe, and H.-S. Park, Nature Physics **11**, 173 (2015).

[34] L. Willingale, A. G. R. Thomas, P. M. Nilson, M. C. Kaluza, S. Bandyopadhyay, A. E. Dangor, R. G. Evans, P. Fernandes, M. G. Haines, C. Kamperidis, R. J. Kingham, S. Minardi, M. Notley, C. P. Ridgers, W. Rozmus, M. Sherlock, M. Tatarakis, M. S. Wei, Z. Najmudin, and K. Krushelnick, Physical Review Letters **105** (2010), 10.1103/physrevlett.105.095001.

ACCEPTED MANUSCRIPT
Review of Scientific Instruments
This is the author's peer reviewed, accepted manuscript. However, the online version of record will be different from this version once it has been copyedited and typeset.
PLEASE CITE THIS ARTICLE AS DOI:10.1063/1.5123392
AIP Publishing

[35] L. Lancia, B. Albertazzi, C. Boniface, A. Grisollet, R. Riquier, F. Chaland, K.-C. L. Thanh, P. Mellor, P. Antici, S. Buffechoux, S. Chen, D. Doria, M. Nakatsutsumi, C. Peth, M. Swantusch, M. Stardubtsev, L. Palumbo, M. Borghesi, O. Willi, H. Pépin, and J. Fuchs, Physical Review Letters **113** (2014), 10.1103/physrevlett.113.235001.

[36] L. Gao, P. Nilson, I. Igumenshchev, M. Haines, D. Froula, R. Betti, and D. Meyerhofer, Physical Review Letters **114** (2015), 10.1103/physrevlett.114.215003.

[37] P. Tzeferacos, A. Rigby, A. F. A. Bott, A. R. Bell, R. Bingham, A. Casner, F. Cattaneo, E. M. Churazov, J. Emig, F. Fiuza, C. B. Forest, J. Foster, C. Graziani, J. Katz, M. Koenig, C.-K. Li, J. Meinecke, R. Petrasso, H.-S. Park, B. A. Remington, J. S. Ross, D. Ryu, D. Ryutov, T. G. White, B. Reville, F. Miniati, A. A. Schekochihin, D. Q. Lamb, D. H. Froula, and G. Gregori, Nature Communications **9** (2018), 10.1038/s41467-018-02953-2.

[38] P. Tzeferacos, A. Rigby, A. Bott, A. R. Bell, R. Bingham, A. Casner, F. Cattaneo, E. M. Churazov, J. Emig, N. Flocke, F. Fiuza, C. B. Forest, J. Foster, C. Graziani, J. Katz, M. Koenig, C.-K. Li, J. Meinecke, R. Petrasso, H.-S. Park, B. A. Remington, J. S. Ross, D. Ryu, D. Ryutov, K. Weide, T. G. White, B. Reville, F. Miniati, A. A. Schekochihin, D. H. Froula, G. Gregori, and D. Q. Lamb, Physics of Plasmas **24**, 041404 (2017).

[39] N. Sinenian, M. J. Rosenberg, M. Manuel, S. C. McDuffee, D. T. Casey, A. B. Zylstra, H. G. Rinderknecht, M. G. Johnson, F. H. Séguin, J. A. Frenje, C. K. Li, and R. D. Petrasso, Review of Scientific Instruments **82**, 103303 (2011).

[40] K. Flippo, T. Bartal, F. Beg, S. Chawla, J. Cobble, S. Gaillard, D. Hey, A. MacKinnon, A. MacPhee, P. Nilson, D. Offermann, S. L. Pape, and M. J. Schmitt, Journal of Physics: Conference Series **244**, 022033 (2010).

[41] N. L. Kugland, D. D. Ryutov, C. Plechaty, J. S. Ross, and H.-S. Park, Review of Scientific Instruments **83**, 101301 (2012).

[42] A. F. A. Bott, C. Graziani, P. Tzeferacos, T. G. White, D. Q. Lamb, G. Gregori, and A. A. Schekochihin, Journal of Plasma Physics **83** (2017), 10.1017/s0022377817000939.

[43] C. Graziani, P. Tzeferacos, D. Q. Lamb, and C. Li, Review of Scientific Instruments **88**, 123507 (2017).

[44] C. J. Werner, J. S. Bull, C. J. Solomon, F. B. Brown, G. W. McKinney, M. E. Rising, D. A. Dixon, R. L. Martz, H. G. Hughes, L. J. Cox, A. J. Zukaitis, J. C. Armstrong, R. A. Forster, and L. Casswell, *MCNP Version 6.2 Release Notes*, Tech. Rep. (2018).

[45] S. A. et. al., Nuclear Instruments and Methods in Physics Research Section A: Accelerators, Spectrometers, Detectors and Associated Equipment **506**, 250 (2003).

[46] L. Volpe, R. Ramis, S. Baton, P. Nicolai, F. Perez, J. J. Santos, B. Vauzour, D. Batani, and M. Koenig, IEEE Transactions on Plasma Science **40**, 1131 (2012).

[47] M. C. Levy, D. D. Ryutov, S. C. Wilks, J. S. Ross, C. M. Huntington, F. Fiuza, D. A. Martinez, N. L. Kugland, M. G. Baring, and H.-S. Park, Review of Scientific Instruments **86**, 033302 (2015).

[48] M. J.-E. Manuel, A. B. Zylstra, H. G. Rinderknecht, D. T. Casey, M. J. Rosenberg, N. Sinenian, C. K. Li, J. A. Frenje, F. H. Séguin, and R. D. Petrasso, Review of Scientific Instruments **83**, 063506 (2012).

[49] M. J. Turk, B. D. Smith, J. S. Oishi, S. Skory, S. W. Skillman, T. Abel, and M. L. Norman, The Astrophysical Journal Supplement Series **192**, 9 (2010).

[50] B. Fryxell, K. Olson, P. Ricker, F. X. Timmes, M. Zingale, D. Q. Lamb, P. MacNeice, R. Rosner, J. W. Truran, and H. Tufo, The Astrophysical Journal Supplement Series **131**, 273 (2000).

[51] Lu et. al., 2019, in preparation.

[52] M. J. Berger, M. Inokuti, H. H. Andersen, H. Bichsel, D. Powers, S. . M. Seltzer, D. . Thwaites, and D. E. Watt, Journal of the International Commission on Radiation Units and Measurements **os25**, NP (1993).

[53] H. Bethe, Annalen der Physik **397**, 325 (1930).

[54] C.-K. Li and R. D. Petrasso, Physical Review Letters **70**, 3059 (1993).

[55] D. GERICKE, Laser and Particle Beams **20**, 471 (2002).

[56] E. Bonderup and P. Hvelplund, Physical Review A **4**, 562 (1971).

[57] S. Seltzer, "Stopping-powers and range tables for electrons, protons, and helium ions, nist standard reference database 124," (1993).

[58] J. F. Ziegler, M. Ziegler, and J. Biersack, Nuclear Instruments and Methods in Physics Research Section B: Beam Interactions with Materials and Atoms **268**, 1818 (2010).

[59] PROPACEOS is available at http://www.prism-cs.com.

[60] H. A. Bethe, Physical Review **89**, 1256 (1953).

[61] G. Moliere, Zeitschrift fÃŒr Naturforschung A **3**, 78 (1948).

[62] N. Mokhov and S. Striganov, Los Alamos Natl. Lab (2002).

[63] A. S. Liao, S. Li, H. Li, K. Flippo, D. Barnak, K. V. Kelso, C. F. Kawaguchi, A. Rasmus, S. Klein, J. Levesque, C. Kuranz, and C. Li, Physics of Plasmas **26**, 032306 (2019).

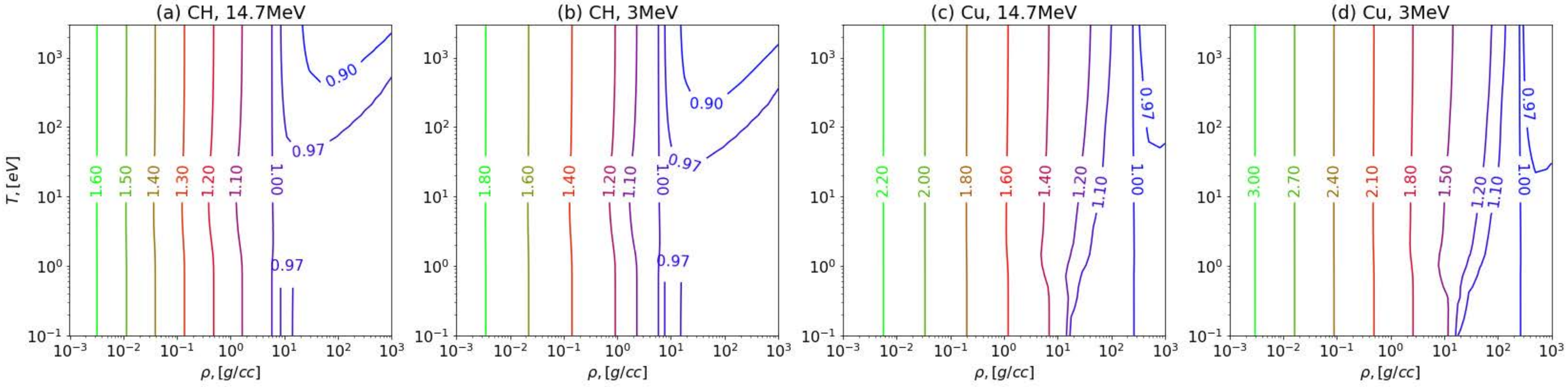
(a) CH, 14.7MeV
(b) CH, 3MeV
(c) Cu, 14.7MeV
(d) Cu, 3MeV
T, [eV]
ρ, [g/cc]
1.60
1.50
1.40
1.30
1.20
1.10
1.00
0.97
0.90
1.80
2.20
2.00
3.00
2.70
2.40
2.10

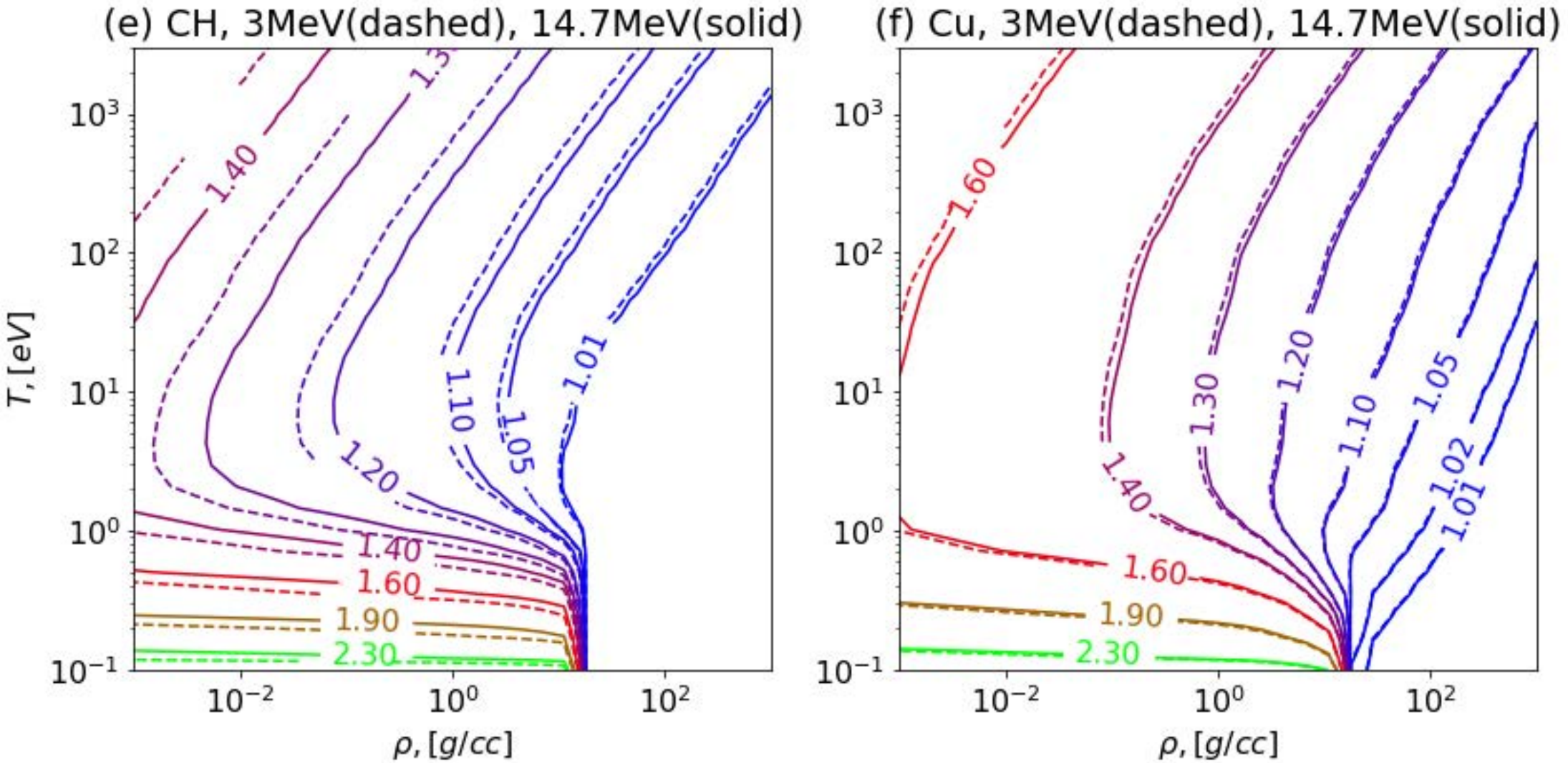
(e) CH, 3MeV(dashed), 14.7MeV(solid)
(f) Cu, 3MeV(dashed), 14.7MeV(solid)
T, [eV]
ρ, [g/cc]
10^3
10^2
10^1
10^0
10^-1
10^-2
1.40
1.20
1.10
1.05
1.01
1.60
1.90
2.30
1.30
1.02

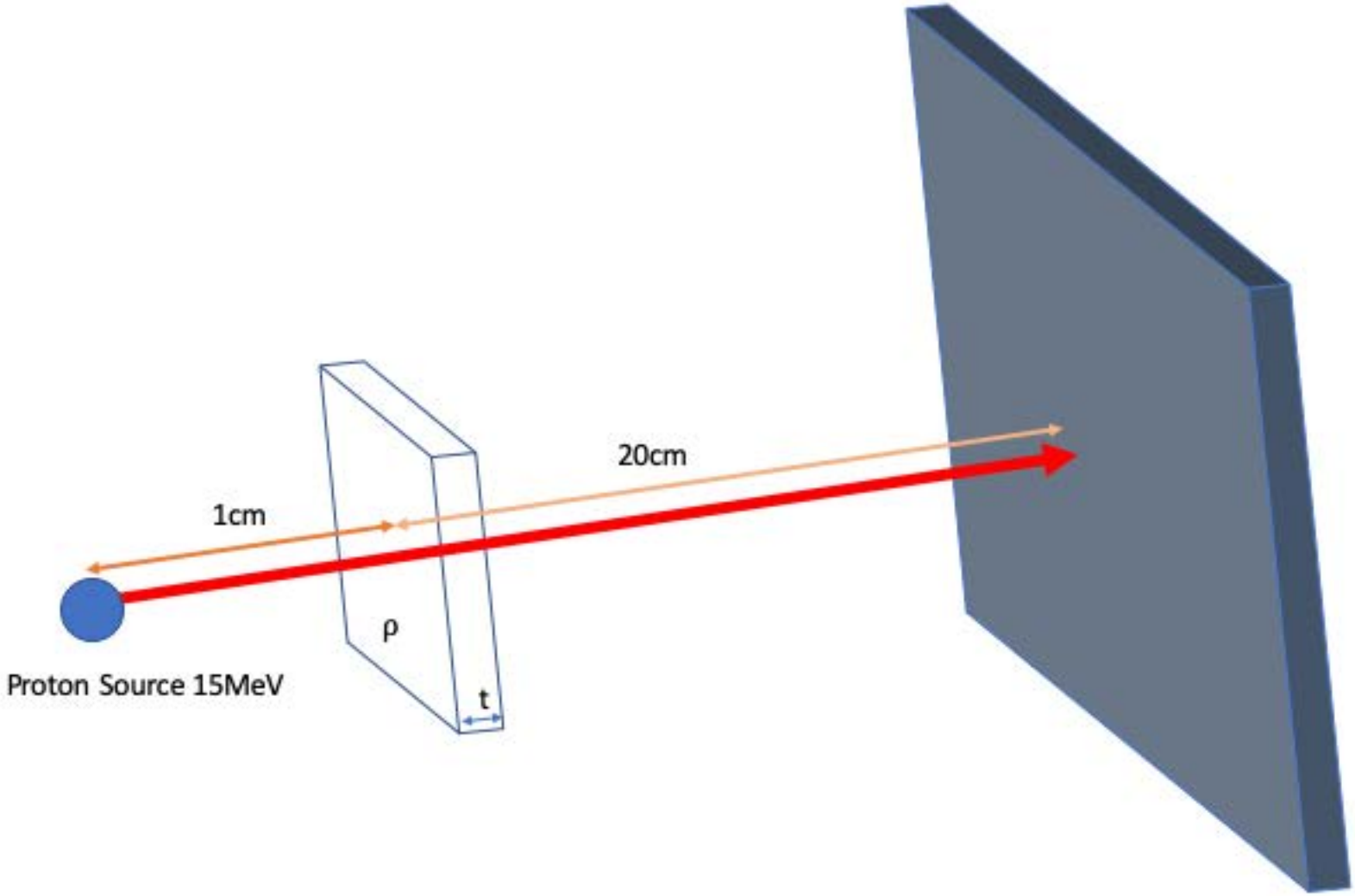
20cm
1cm
ρ
t
Proton Source 15MeV

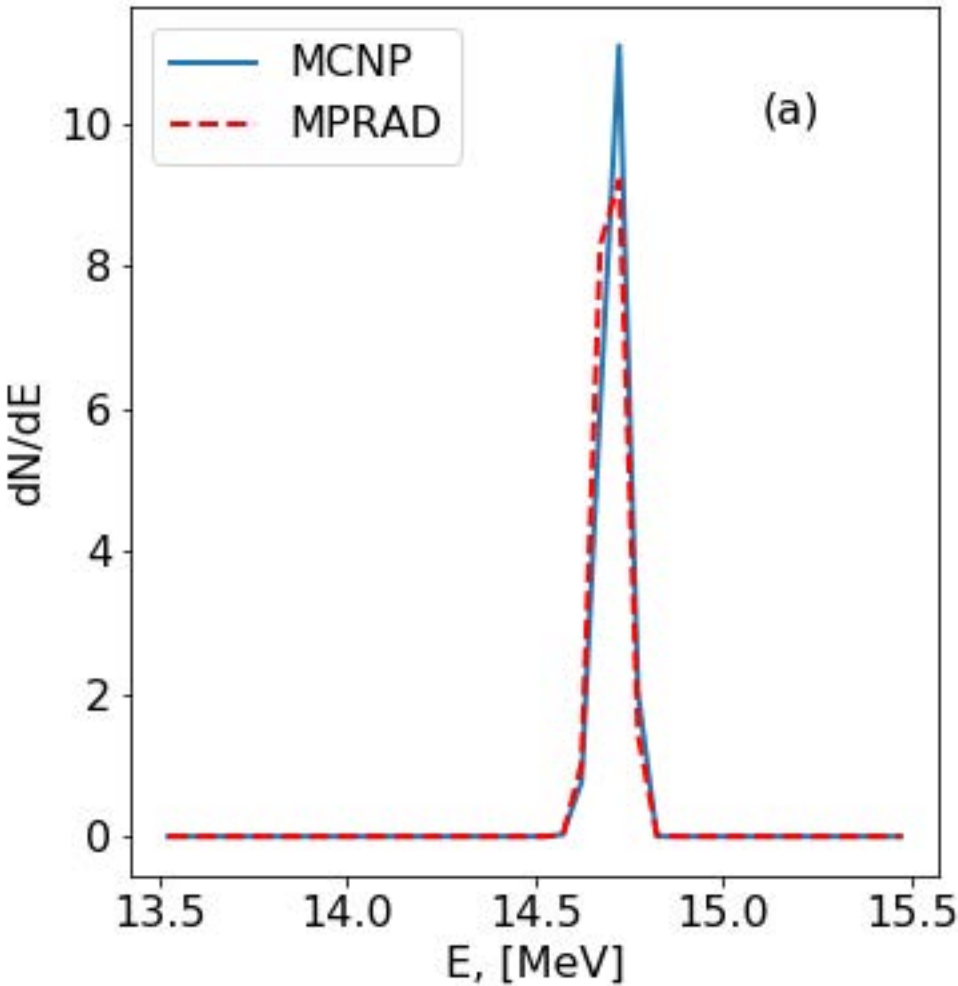
MCNP
MPRAD
(a)
dN/dE
0
2
4
6
8
10
13.5
14.0
14.5
15.0
15.5
E, [MeV]

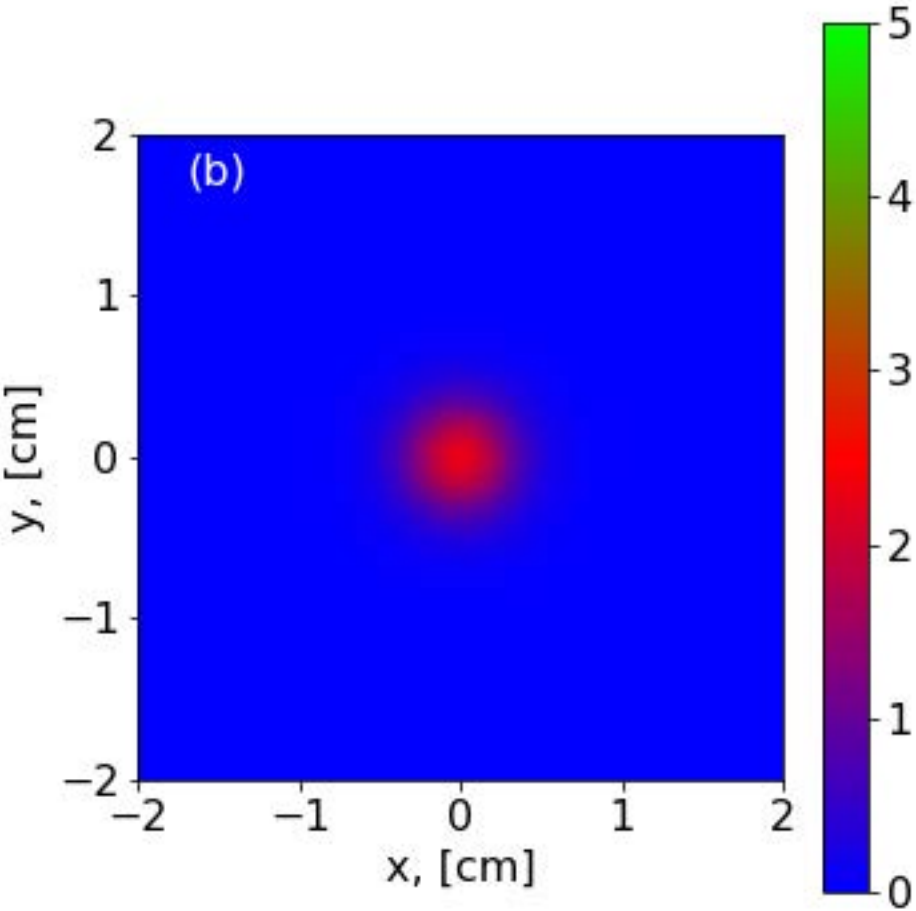
(b)
2
1
0
−1
−2
y, [cm]
−2
−1
0
1
2
x, [cm]
5
4
3
2
1
0

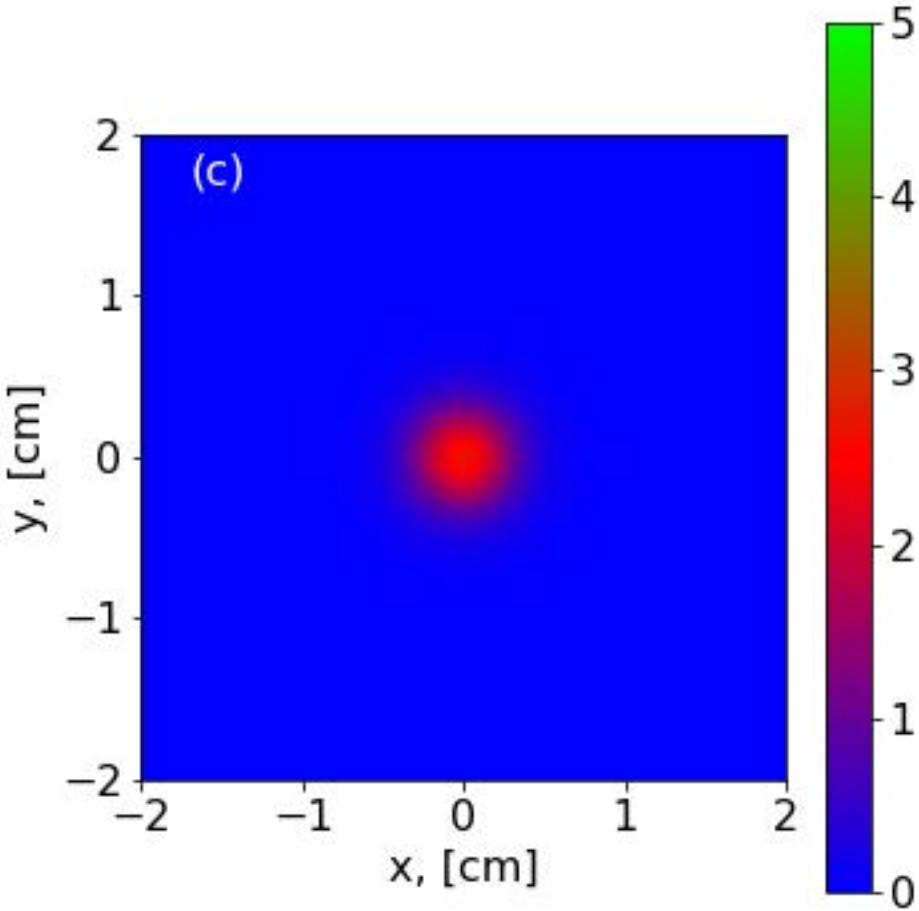
(c)
2
1
0
−1
−2
y, [cm]
−2
−1
0
1
2
x, [cm]
5
4
3
2
1
0

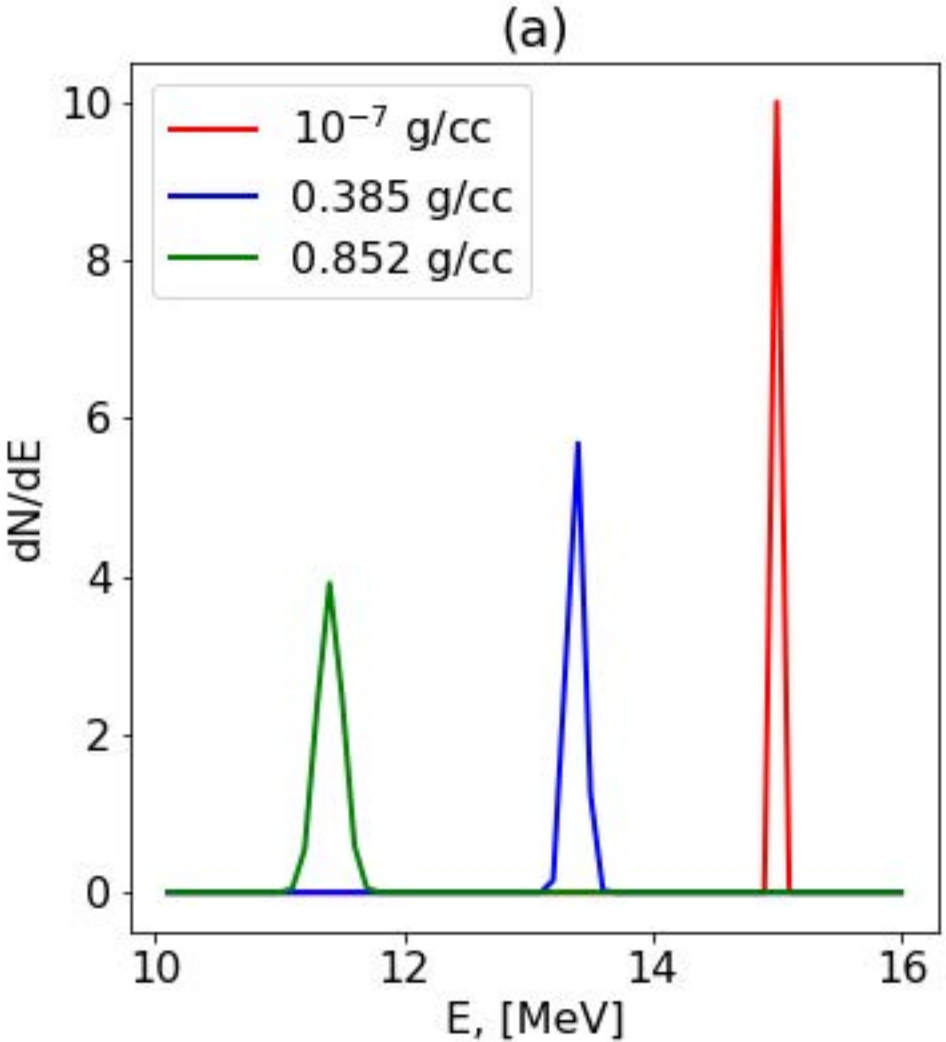
(a)
10^{-7} g/cc
0.385 g/cc
0.852 g/cc
dN/dE
E, [MeV]
0
2
4
6
8
10
10
12
14
16

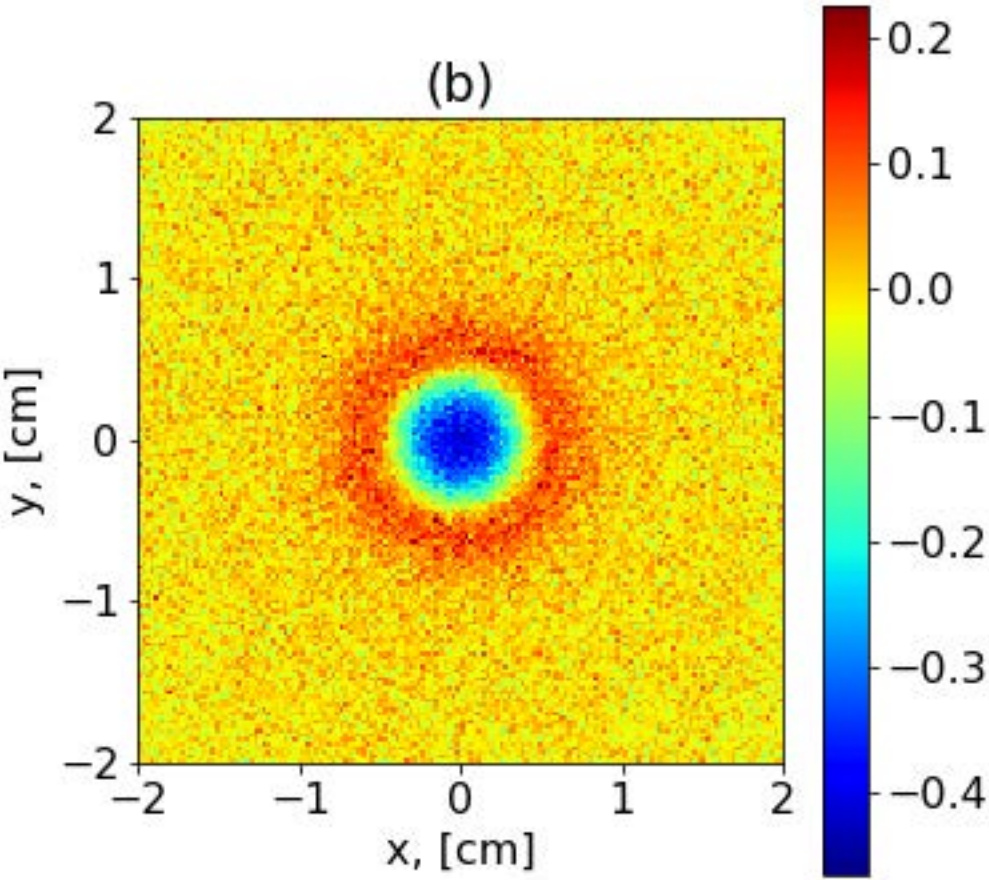
(b)
2
1
0
−1
−2
y, [cm]
−2
−1
0
1
2
x, [cm]
0.2
0.1
0.0
−0.1
−0.2
−0.3
−0.4

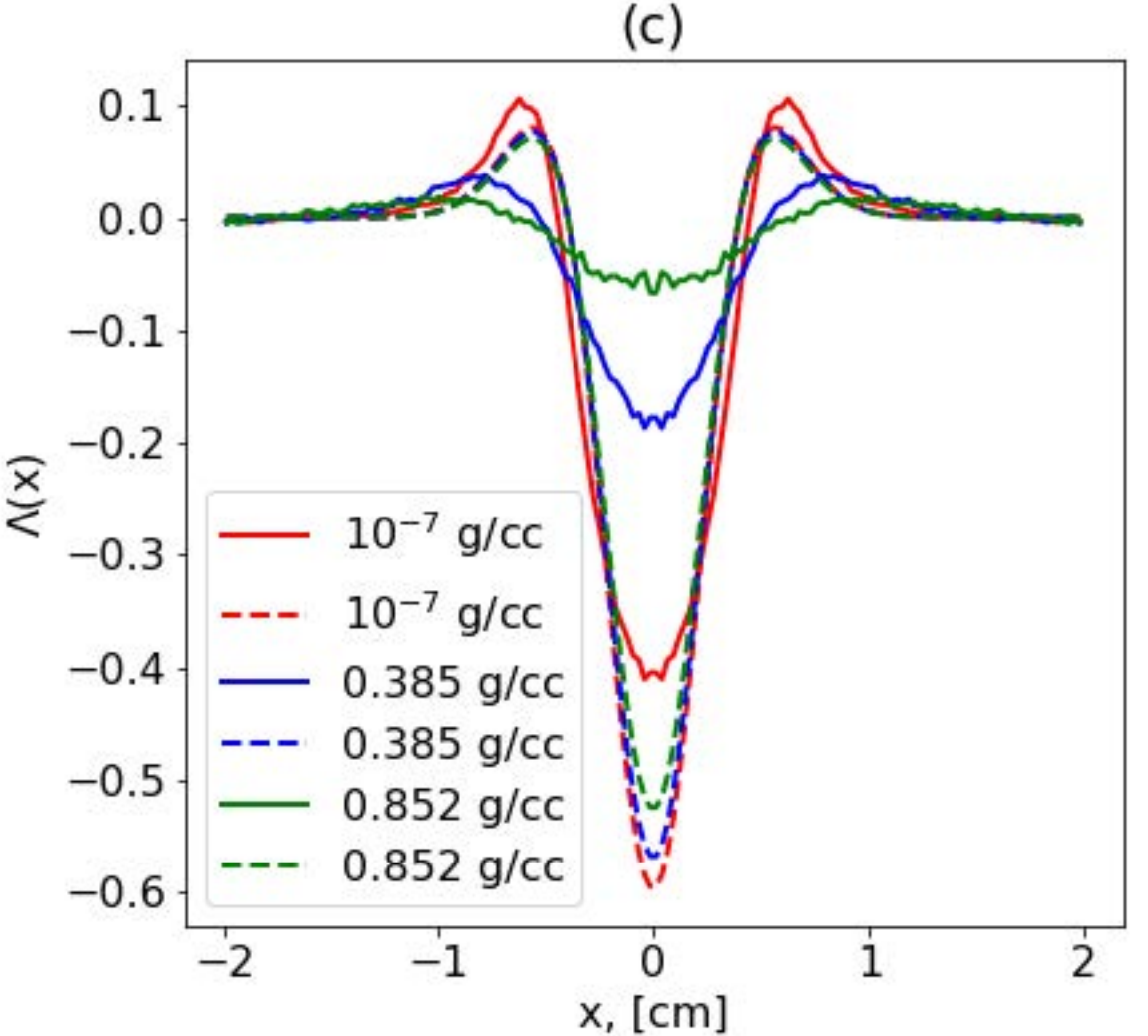
(c)
0.1
0.0
−0.1
−0.2
−0.3
−0.4
−0.5
−0.6
Λ(x)
−2
−1
0
1
2
x, [cm]
10⁻⁷ g/cc
10⁻⁷ g/cc
0.385 g/cc
0.385 g/cc
0.852 g/cc
0.852 g/cc

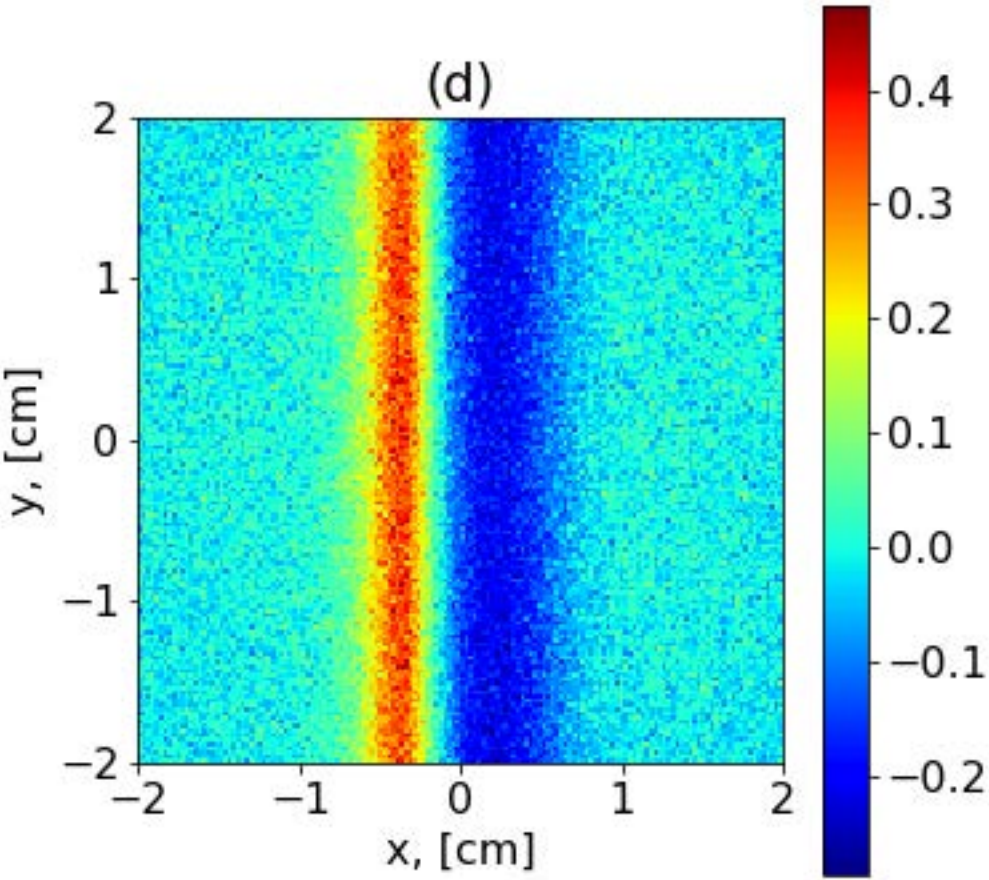
(d)
2
1
0
−1
−2
y, [cm]
−2
−1
0
1
2
x, [cm]
0.4
0.3
0.2
0.1
0.0
−0.1
−0.2

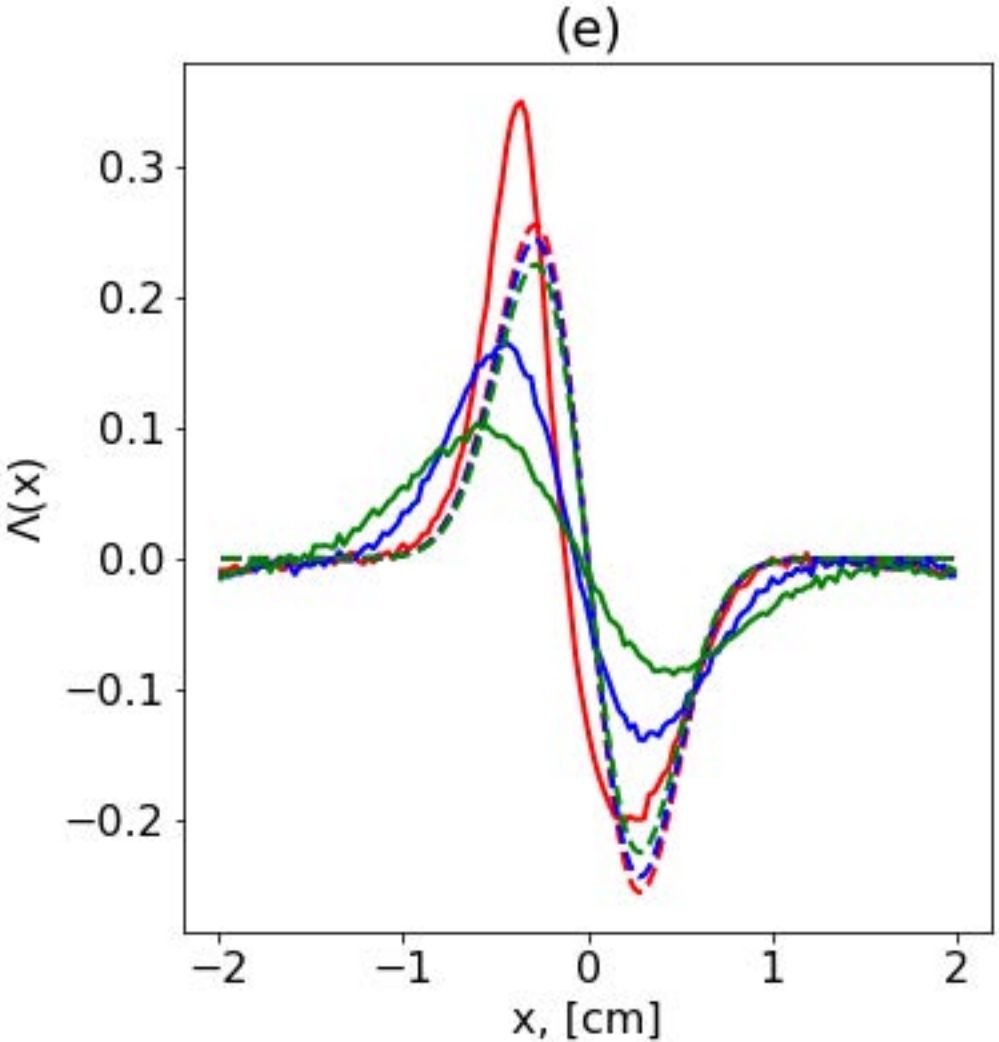
(e)
0.3
0.2
0.1
0.0
−0.1
−0.2
Λ(x)
−2
−1
0
1
2
x, [cm]

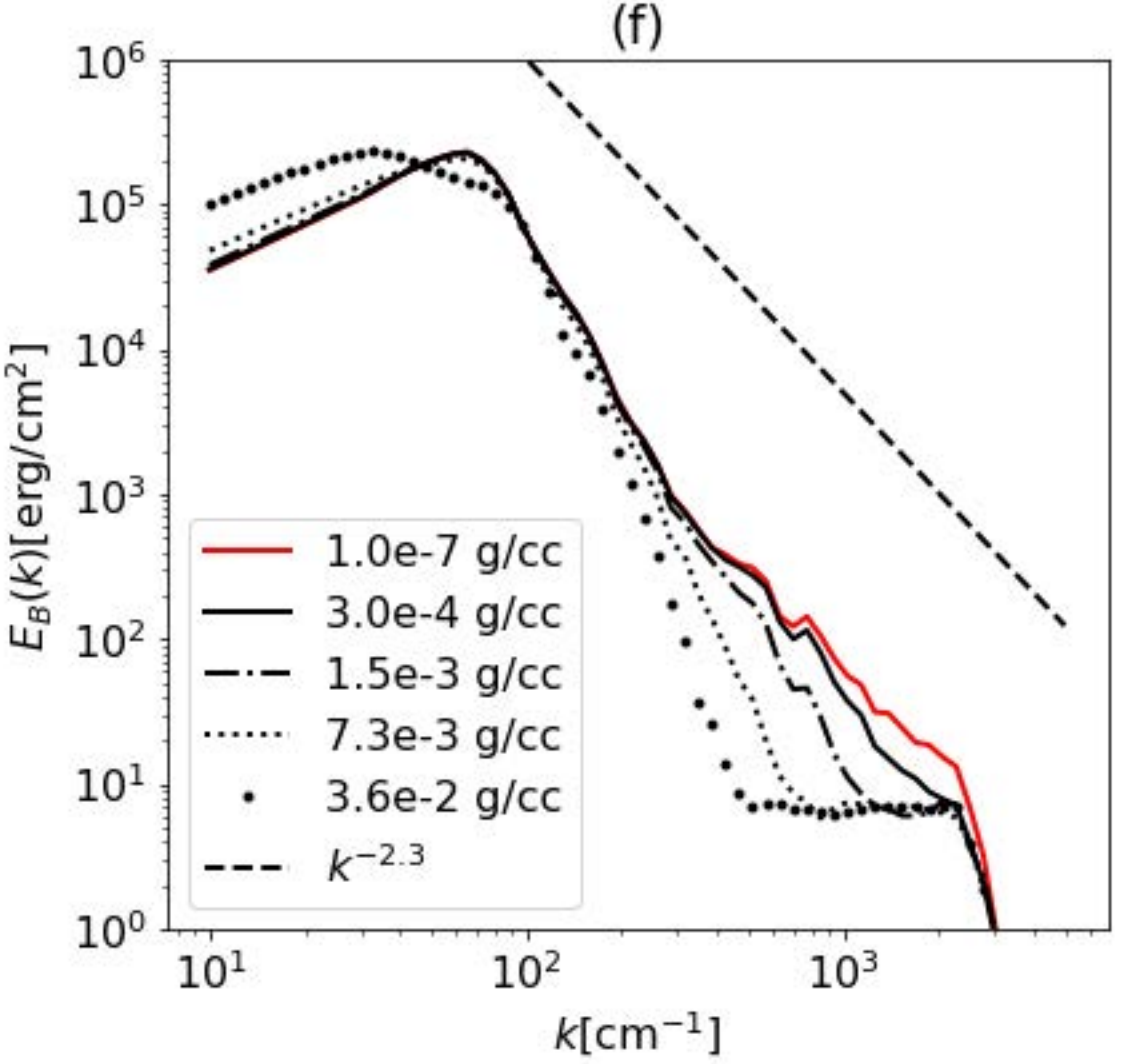
(f)
10^6
10^5
10^4
10^3
10^2
10^1
10^0
$E_B(k)$[erg/cm^2]
1.0e-7 g/cc
3.0e-4 g/cc
1.5e-3 g/cc
7.3e-3 g/cc
3.6e-2 g/cc
$k^{-2.3}$
10^1
10^2
10^3
k[cm^{-1}]